J. Fluid Mech. (2006), *vol.* 566, *pp.* 195–224.
doi:10.1017/S0022112006001923 Printed in the United Kingdom

Three-dimensional transition of a water flow around a heated cylinder at $Re = 85$ and $Ri = 1.0$

By MAOSHENG REN, CAMILO C. M. RINDT AND ANTON A. VAN STEENHOVEN

Laboratory for Energy Technology, Department of Mechanical Engineering, Technische Universiteit Eindhoven, PO Box 513, 5600 MB Eindhoven, The Netherlands

(Received 29 June 2005 and in revised form 3 April 2006)

The three-dimensional flow transition behind a heated cylinder subjected to a horizontal flow (water is used as the working fluid; $Pr \simeq 7$) at a Reynolds number $Re = 85$ and a Richardson number $Ri = 1.0$, manifests itself in the far wake as escaping mushroom-type structures from the upper vortices. The origin of the escaping mushroom-type structures lies in the generation of streamwise vorticity in the near wake, which is described as a cyclic process. In the presence of a spanwise temperature gradient in the near wake, streamwise vorticity is generated, which results from baroclinic vorticity production. Owing to these streamwise vorticity regions, low-speed flow will move upwards at so-called in-plume positions resulting in high- and low-speed streaks in the upper half of the wake. Next, 'transverse' vorticity is generated by the spanwise gradients in the streamwise velocity component, resulting in counter-rotating vortices directly behind the cylinder. These vortices lead to high- and low-temperature regions in the spanwise direction and the process repeats itself.

1. Introduction

Over the last fifteen years, much attention has been paid to the three-dimensional vortex dynamics behind a cylinder. Experimental and theoretical studies of the three-dimensional wake transition significantly contributed to the understanding of this dynamics (Huerre & Monkewitz 1990; Mittal & Balachander 1995; Williamson 1996*a*, *b*). Studies on the instability mechanisms resulting in the formation of two-dimensional and three-dimensional vortical structures, can contribute to better understanding of laminar–turbulent transition and may lead to ways of actively controlling the features of the flow.

Although mixed convection around bluff bodies is of great importance for various engineering applications (electronics cooling, compact heat exchangers), wake stability for a heated cylinder has until now received little attention compared to the forced convection case. In the early 1970s, this effect was investigated to determine the global effects of the induced heat on the heat exchange coefficient (Hatton, James & Swire 1970). It turned out that for a Richardson number larger than 0.2, the heat transfer coefficient was influenced considerably by the thermally induced flow. These investigations, were carried out for various angles between the gravity vector and the main flow direction, and resulted in a set of critical Richardson numbers above which thermal effects influence the heat exchange coefficient. In the investigations, the circumstances could be established at which hot-wire velocity measurements could be applied, but almost no attention was paid to the effect of heat on the wake structures and wake behaviour.

More detailed studies on the effect of heat on the vortex wake were carried out slightly later (Noto, Ishida & Matsumoto 1985; Noto & Matsumoto 1987; Badr 1984) and some remarkable results were obtained. These studies describe the flow around a heated horizontal cylinder exposed to a vertically directed flow. By increasing the heat input (increasing the Richardson number), the Strouhal number first increases. However, above a critical Richardson number, the Strouhal number becomes zero and vortex shedding is suppressed. For this heat input, the vortex street converts again to a wake in which twin vortices are situated in the near wake. A further increase of the heat input causes these vortices to disappear, ending up with a thermal plume. The influence of buoyancy on the vortex-shedding frequency was further analysed numerically by Chang & Sa (1990). The same results were obtained in experiments performed by Michaux-Leblond & Bélorgey (1997) and here the dualism between buoyancy and viscous effects was considered to be the source of the sudden disappearance of the vortex-shedding phenomenon.

The non-parallelism between the crossflow direction and the buoyancy force causes the flow pattern to become asymmetric, with the vortices in the upper vortex row having slightly different characteristics to the vortices in the lower row. The effect of the angle between the main flow and the gravity direction was numerically investigated with two-dimensional calculations by Noto (1991). From this study it was found that the angle of attack has a major influence on the vortex street characteristics. Starting with an angle of 180° (corresponding to a vertical upward flow) it was found that first the vortex shedding was suppressed by an increasing heat addition. When the angle of attack was decreased, the wake became periodic again, while for angles smaller than 90°, the natural frequency was found to become even larger than for the unheated situation.

For a horizontally mounted cylinder and in the case of air, the vortex shedding can be suppressed by heating of the cylinder at Reynolds values just above the critical value: $Re_c = 49$ (Lecordier, Hamma & Paranthoen 1991; Wang, Travnicek & Chia 2000). In Lecordier *et al.* (2000), the sudden disappearance of the vortex-shedding phenomenon is analysed and it is concluded that the influence of temperature on the viscosity is the primary source. In fact, an increase of temperature leads to a decrease of the effective Reynolds number. However, for water, the opposite holds because of the different temperature dependency of the viscosity. Kieft, Rindt & van Steenhoven (2002) and van Steenhoven & Rindt (2003) showed the effect of heat input on the behaviour of the coherent structures behind a cylinder at low Reynolds numbers. For Reynolds numbers around 80, Kieft *et al.* (2003) found that, by heating the cylinder, the vortices in the upper and lower rows acquire different strengths owing to baroclinic vorticity production. This strength difference increases for increasing Richardson number. It is observed that, for small Richardson numbers, the shed vortices move slightly downwards.

For an unheated cylinder, Williamson's visualizations (1988) showed two modes of small-scale three-dimensional instability. The two different modes scale on different features of the flow. For Reynolds numbers larger than 180–190, the mode A instability has a spanwise wavelength of 4 cylinder diameters. Mode A appears to be linked to an elliptical instability of the primary vortex core during the process of shedding, which causes a spanwise waviness (Williamson 1996*a*). The term 'elliptical instability' is the name given to the linear instability mechanism by which three-dimensional flow can be generated in regions of elliptical streamlines (Pierrehumbert 1986; Waleffe 1990). At each spanwise location where the vortex is displaced upstream towards the cylinder, the vortex becomes highly deformed by the strain-rate field, and part of the vortex

Three-dimensional transition	Reynolds number	Richardson number	Wavelength
Mode A, Williamson (1996*b*)	180–230	0	4*d*
Mode B, Williamson (1996*b*)	200–280	0	1*d*
Mode E	75–117	0.35–2.5	2*d*

TABLE 1. The different modes of three-dimensional transition in the cylinder wake flow. The ranges indicated for mode E are based on visualization results. Mode E is investigated in the present study at one Reynolds and Richardson number.

is pulled back towards the cylinder, forming a vortex loop. This vortex formation is related to streamwise vorticity stretching in the regions between the primary vortices. However, other workers believe that the streamwise vortices are a manifestation of Görtler vortices (Brede, Eckelmann & Rockwell 1996). They suggested that the origin of the streamwise vorticity may come from the centrifugal instability near the braid regions.

For Reynolds numbers larger than 230–260, a mode B transition occurs with a spanwise wavelength of around 1 cylinder diameter. The mode B instability is related to an instability of the shear layer in the braid region. In addition to the mode A and mode B transitions, Zhang *et al.* (1995) found a mode C transition with a spanwise wavelength of 1.8 cylinder diameters. Mode C usually appears for $170 < Re < 270$ only if mode A and mode B are inhibited from developing by a thin control-wire placed parallel to the cylinder in the near wake.

For a heated cylinder in water, Maas, Rindt & van Steenhoven (2003) showed that a three-dimensional transition in the wake flow occurs at a Reynolds number lower than for the unheated case. Escaping mushroom-type structures occur in the far-wake with a spanwise distance of around twice the cylinder diameter (Ren, Rindt & van Steenhoven 2004*a*). Furthermore, it has also been shown that the vortex formation shows large differences between the 'in-plume' position (where the plume escapes further downstream) and the 'out-of-plume' position. The shedding process for the 'out-of-plume' position is similar to that for an unheated cylinder. For the 'in-plume' positions, the formation of the saddle point in the upper and lower side of the wake is not symmetrical in one vortex-shedding cycle. Furthermore, at the 'in-plume' positions, an upward motion occurs directly behind the cylinder, which separates the vortices from the cylinder wall. An upward motion near the cylinder wall enhances the formation of the upper vortices and weakens the formation of the lower ones (Ren *et al.* 2004*a*).

To distinguish the three-dimensional transition occurring for mixed convection from the other transition modes, this mode is denoted as 'mode E'. As shown in figure 4(*a*), mushroom-type structures escape from the upper vortices. Moreover, the mode E transition occurs at a much lower Reynolds number than modes A and B for the unheated case. Table 1 shows the length scales of the different modes of three-dimensional transition. It seems, from the jump in length scales, that there exist different kinds of three-dimensional transition mechanisms. The mode E transition is different from modes A and B, since the heating brings asymmetry into the wake formation behind a horizontal cylinder.

The current investigation focuses on the flow phenomena behind a heated cylinder subjected to a horizontal water flow at one Reynolds number and one Richardson number, $Re = 85$ and $Ri = 1.0$, respectively. The goal of this study is to gain more insight into the 'mode E' transition mechanism. It has been observed from visualization

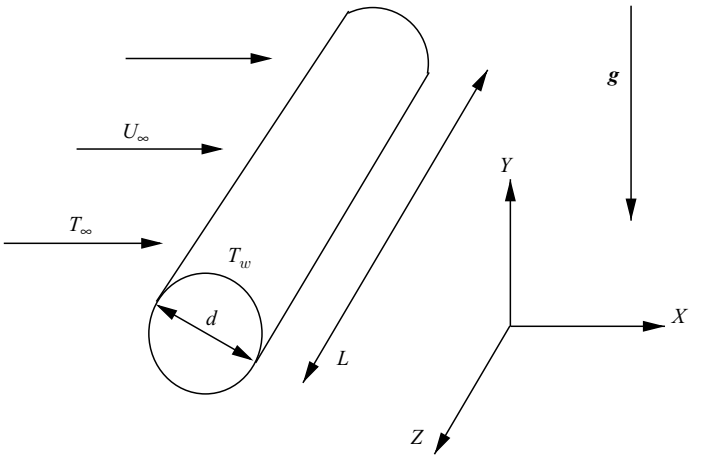

FIGURE 1. Problem definition: the cylinder, positioned at $x = 0$ and $y = 0$, has a temperature T_w and is subject to a horizontal crossflow with velocity U_∞ and temperature T_∞ and gravity is in negative y-direction.

results that the flow features of mode E transition are similar within the range of Reynolds numbers $75 < Re < 117$ and Richardson numbers $0.35 < Ri < 2.5$ studied. Therefore, the transition process as described in detail for the situation under consideration here may also hold for other Reynolds and Richardson numbers in the regime mentioned. Both experimental and numerical techniques are used, including an electro-chemical tin-precipitation visualization method, a high-resolution particle velocimetry and a three-dimensional spectral element method (SEM). The paper is organized as follows. First, a description of the problem definition is given, together with the experimental set-up and investigation techniques. Then, the three-dimensional-transition mechanism is proposed behind a heated cylinder. Next, the formation process of the secondary vortical structures is analysed in the near wake. Finally, the main conclusions are given.

2. Methodology

2.1. *Problem definition*

In the current investigation the three-dimensional transition behind a heated cylinder is investigated at low Reynolds numbers. The cylinder is exposed to a horizontal uniform crossflow (figure 1) where the z-axis is in the spanwise direction, the x-axis in the streamwise direction, and the y-axis in the negative gravity direction. The cylinder is positioned at $x = 0$ and $y = 0$.

In the calculations, the flow is assumed to obey the Boussinesq approximation; the density variations are negligible except in the buoyancy force. For a small temperature difference, the Boussinesq approximation is believed to give good results. This paper focuses on $Re = 85$ and $Ri = 1.0$ and the corresponding temperature difference then is $T_w - T_\infty \simeq 5.7\,^\circ\mathrm{C}$, using water as the working fluid. With use of the Boussinesq approximation in the numerical simulation, the flow structures and transition mechanism have been identified. Furthermore, the experiments and calculations are quantitatively compared in Ren *et al.* (2004*a*), which validates the calculation approach. There, a good agreement has been achieved between the

experimentally measured and numerically calculated velocity fields in the (X,Y)-plane at in-plume and out-of-plume positions.

The dimensionless conservation equations for mass, momentum and energy are, respectively:

$$\nabla \cdot \boldsymbol{u} = 0, \tag{2.1}$$

$$\frac{\partial \boldsymbol{u}}{\partial t} + \boldsymbol{u} \cdot \nabla \boldsymbol{u} = -\nabla p + \frac{1}{Re}\nabla^2 \boldsymbol{u} - Ri\, \Theta\, \boldsymbol{g}, \tag{2.2}$$

$$\frac{\partial \Theta}{\partial t} + \boldsymbol{u} \cdot \nabla \Theta = \frac{1}{Re\, Pr}\nabla^2 \Theta, \tag{2.3}$$

with $Re = U_\infty d/\nu$ the Reynolds number (U_∞ upstream velocity, d cylinder diameter and ν kinematic viscosity), $Ri = Gr/Re^2 = g\beta(T_w - T_\infty)d/U_\infty^2$ the Richardson number (T_∞ upstream temperature and T_w cylinder temperature), $Gr = g\beta(T_w - T_\infty)d^3/\nu^2$ the Grashof number, $Pr = \nu/\kappa$ the Prandtl number, β the thermal expansion coefficient, κ the thermal diffusivity, g the gravity constant, $\boldsymbol{g} = (0, -1, 0)^T$ the dimensionless gravity vector, $\Theta = (T - T_\infty)/(T_w - T_\infty)$ the dimensionless temperature, $\boldsymbol{u}$ the dimensionless velocity and p the dimensionless pressure. From these dimensionless conservation equations with suitable boundary conditions, we can conclude that the character of the flow depends on the dimensionless parameters Re, Ri and Pr. In the current investigation, the flow phenomena are studied at $Re = 85$ and $Ri = 1.0$. Because water is used as the working fluid, the Prandtl number is more or less constant, around 7.

The vorticity transport equation can be obtained by taking the curl of the momentum equation (2.2) and an equation for the rate of change of vorticity is then derived:

$$\frac{\partial \boldsymbol{\omega}}{\partial t} + \boldsymbol{u} \cdot \nabla \boldsymbol{\omega} = (\boldsymbol{\omega} \cdot \nabla)\boldsymbol{u} + \frac{1}{Re}\nabla^2 \boldsymbol{\omega} - Ri\, \nabla\Theta \times \boldsymbol{g}. \tag{2.4}$$

The left-hand side of equation (2.4) represents the rate of change of vorticity while moving with the fluid. The term $(\boldsymbol{\omega} \cdot \nabla)\boldsymbol{u}$ represents the rate of change of $\boldsymbol{\omega}$ due to stretching and tilting of vortex lines, the term $(1/Re)\nabla^2\boldsymbol{\omega}$ the rate of change of $\boldsymbol{\omega}$ due to diffusion of vorticity, and the term $Ri\,\nabla\Theta \times \boldsymbol{g}$ the rate of generation of $\boldsymbol{\omega}$ due to baroclinicity of the flow.

2.2. *Experimental set-up*

The apparatus used in the experiment consists of three parts: the water tank, the light source with illumination system, and the image recording with post-processing system.

The flow is investigated in a so-called towing tank configuration, as shown in figure 2, with dimensions $length \times width \times height = 500 \times 50 \times 75\,\mathrm{cm}^3$. In this configuration, the cylinder is towed through the water with a constant velocity U_∞. The cylinder has length $L = 495$ mm and diameter $d = 8.5$ mm (aspect ratio $L/d = 58$). The test section consists of 15 mm glass windows, held together by a steel frame, so the towing tank is optically accessible from all directions. The cylinder is positioned between two Perspex plates, which are connected to a stiff structure, which also carries the measurement equipment, like cameras and light sources. The stiff construction can be translated along two rails that are mounted on top of the water tank. The Perspex plates are constructed in such a way that minimum disturbances are created and oblique vortex shedding is suppressed. A cylindrical heating element with diameter 6.35 mm is used to obtain the desired cylinder wall temperature. The whole of the tank is supported by a sturdy steel framework and is situated in a temperature-controlled laboratory. A detailed description of the towing tank is given in Kieft (2000).

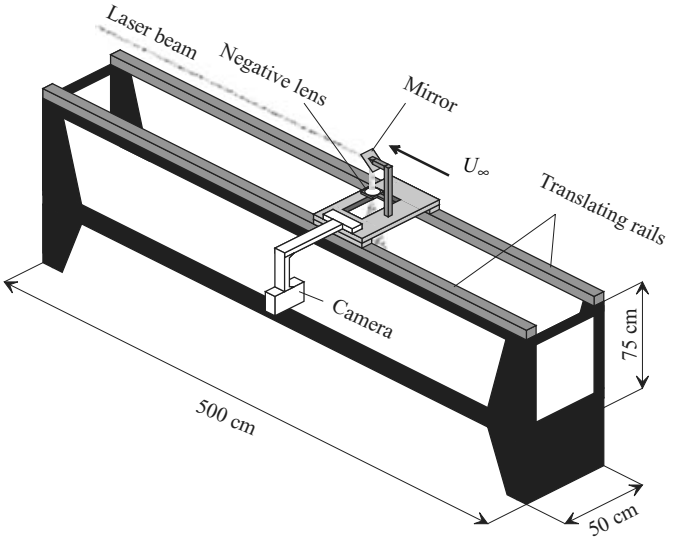

FIGURE 2. Experimental set-up. In this configuration the cylinder is towed through the water with a constant velocity U_∞.

The light source is a pulsed neodymium: yttrium-aluminium-garnet (Nd:YAG) laser emitting light with a wavelength of 532 nm. One laser pulse has a duration of 6 ns and a maximum energy of 200 mJ. The laser beam is directed parallel to the bottom of the water tank (figure 2). The beam passes a negative lens to form a thin horizontal laser sheet cutting the centreline of the cylinder. The camera is positioned perpendicular to this sheet. The recording is performed by a CCD camera (Kodak Megaplus, 10-bit ES 1.0, 1008 $\times$ 1019 pixels). The camera records images at a maximum frame rate of 29 Hz, which is much larger than the vortex-shedding frequency of 0.166 for $Re = 85$ and $Ri = 1$. A Nikon lens with a focal distance of 50 cm is used in front of the CCD camera. A detailed description of the image recording and post-processing system is given in Ren (2005).

2.3. *Experimental methods*

2.3.1. *Visualization method*

Flow visualizations are carried out using an electro-chemical tin-precipitation method (Honji, Taneda & Tatsuno 1980). In this method tin ions are separated from an anode, by applying a voltage difference. In the current set-up, a thin tin wire, which is used as an anode, is positioned upstream of the cylinder. Because the tin ions do not dissolve in pH-neutral water, the small tin hydroxide particles of O (1 μm) form a homogeneous sheet that moves towards the cylinder. With this sheet the wake behind the cylinder is visualized.

2.3.2. *High-resolution particle velocimetry*

For the velocity measurements of the wake flow, a high-resolution particle velocimetry (HPV) technique is applied. HPV is a combination of particle tracking velocimetry (PTV) and particle image velocimetry (PIV). In the current investigation, hollow spherical particles of size 20 μm are used as seeding. These particles are illuminated with the Nd:YAG pulsed laser. The particles are tracked in three successive images (or more) to obtain their trajectories. The velocity of a particle in the second image is then given by the derivative of the particle position along its trajectory. The

temporal accuracy is much better than for classical PIV. The spatial precision is also very good. A detailed description of the algorithm is presented in Bastiaans, van der Nas & Kieft (2002).

From the particle path, the velocity vector of the particle is calculated at certain positions and times. Since the velocity vectors are randomly distributed, they have to be interpolated onto a regular grid of points. A Gaussian weight function interpolation scheme is used in the current application, in order to calculate the vorticity field. The optimum width of the interpolation window was found to be proportional to the number of seeded vectors. Currently, the width of the interpolation window is between 15 and 30 pixels (Ren, Rindt & van Steenhoven 2004*b*).

2.3.3. *Three-dimensional spectral element method*

Besides the visualization experiments, three-dimensional numerical simulations were performed. For an efficient temporal discretization of equations (2.1)–(2.3), a splitting operation on the convection–diffusion equations is applied (Maday, Paterta & Ronquist 1990). As a result, the convection and the diffusion operators are treated separately. For the momentum equation, in combination with the continuity equation, a pressure correction method is applied. This results in three steps, which account for the convection, diffusion and pressure terms, respectively. The convection equation is integrated forward in time by an explicit third-order Taylor–Galerkin scheme, which comprises three explicit time steps within one implicit time step. The diffusion equation is discretized by an implicit second-order backwards difference scheme. The pressure term is treated by a projection method. Because of the limitation of memory storage, an iterative technique is used and the linear system is solved based on a pre-conditioning conjugate gradient method (Cuvelier, Segal & van Steenhoven 2001). The energy equation is solved in a similar way.

For the spatial discretization, a high-order spectral element method (SEM) is used (Karniadakis & Triantafyllou 1992). The SEM can be considered as a mixture of a finite element method and a spectral method. The principle of SEM is straightforward. Within an element, the equations are discretized using a high-order spectral method. Combining the solutions obtained in all these elements results in the solution on the whole domain. Furthermore, special consideration has been given to the continuity of the solution over the element boundaries. The decomposition of the domain into elements gives the method the geometric flexibility. By using high-order approximation functions within one element, a spectral convergence rate and small numerical errors, such as numerical dispersion and diffusion, can be achieved. More information on the validation of the numerical scheme can be found in Timmermans, Miner & van der Vosse (1996).

The element distribution used in the calculation is shown in figure 3. The boundary conditions are prescribed as follows. At the inlet and cylinder wall, Dirichlet boundary conditions are applied for all three velocity components and the temperature. The normal velocity and the tangential stresses at the side, top and bottom walls are set to zero. Also, the temperature is set to zero here. At the domain outlet, homogeneous Neumann conditions are prescribed for the normal and tangential velocity components as well as for the temperature. The boundary conditions for the pressure correction follow immediately from the global mass conservation. This implicitly states that the pressure is near zero at the outflow boundary (Timmermans *et al.* 1996). The vortices leaving the computational domain will be influenced by the applied boundary condition at the outflow boundary; however, van de Vosse, Minev & Timmermans (1995) showed that this influence is hardly noticeable.

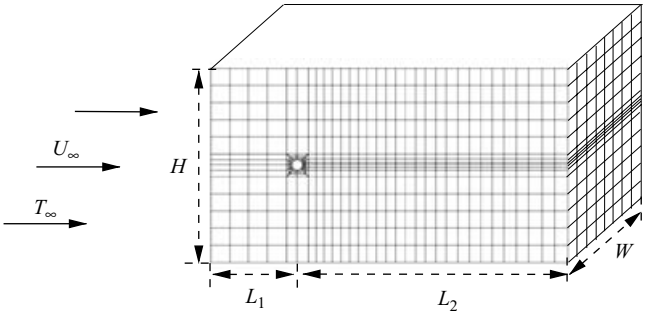

FIGURE 3. Spectral element grid with dimensions $length \times height \times width = 33d \times 18d \times 4d$ ($L_1 = 8$ and $L_2 = 25d$, $H = 18d$, and $W = 4d$), consisting of 1880 elements and 252 315 node points (fifth-order approximation polynomial per element).

The validation is carried out by studying the effect of the domain size and the grid resolution for an unheated flow at $Re = 100$. Two-dimensional flow simulations should adequately reproduce the results of experimental measurements. In the literature, an often-quoted test for the accuracy for cylinder flow computations is the Strouhal number as a function of the Reynolds number. The validation studies show that the Strouhal number increases with decreasing inflow length L_1, decreases with decreasing outflow length L_2, and increases with decreasing domain height H. Similar tendencies have been reported in Karniadakis & Triantafyllou (1992).

In three-dimensional calculations, the solutions are affected by the used span length W of the computational domain. Therefore, the influence of the spanwise length on the coherent structures is studied at $Re = 85$ and $Ri = 1.0$. At these Reynolds and Richardson numbers, previous experimental results indicate that there exists an averaged spanwise wavelength $2d$ (d being the cylinder diameter). The validation studies show that the Strouhal number slightly increases with an increasing span length W. The spanwise wavelength as found from the calculations is more or less fixed by the type of boundary conditions prescribed at the sidewalls and the domain width W. The flow patterns for $W = 2d$ and $W = 4d$ show a spanwise wavelength of $2d$, which is in agreement with the experimental observations of the averaged distance between the mushroom-type structures. For $W = 7d$ and $W = 11d$, a spanwise wavelength is found of around $2.3d$ and $2.2d$, respectively. However, the global flow structures show similar features, such as the escape of the mushroom-type structures from the upper vortices in the far wake. Our results are shown for a computational domain with dimensions $length \times height \times width = 33d \times 18d \times 4d$ ($L_1 = 8d$ and $L_2 = 25d$).

3. Three-dimensional transition mechanism behind a heated cylinder

For an unheated cylinder, for $Re = O(100)$, the wake flow manifests itself as the von Kármán vortex street. The vortex cores are seen as lines parallel to the cylinder. If the heat input is increased, for $Ri \geqslant 1.0$, a three-dimensional transition occurs, which manifests itself as 'mushroom-type' structures (figure 4*b*). These three-dimensional structures escape from the upper vortices in the far wake (figure 4*a*). The spanwise distance between the mushroom-type structures, observed by a top-view visualization, is found to be around $2d$ (figure 4*b*). Since the characteristic length of the flow field is associated with the cylinder diameter, in the remainder of the text all dimensions are scaled with d.

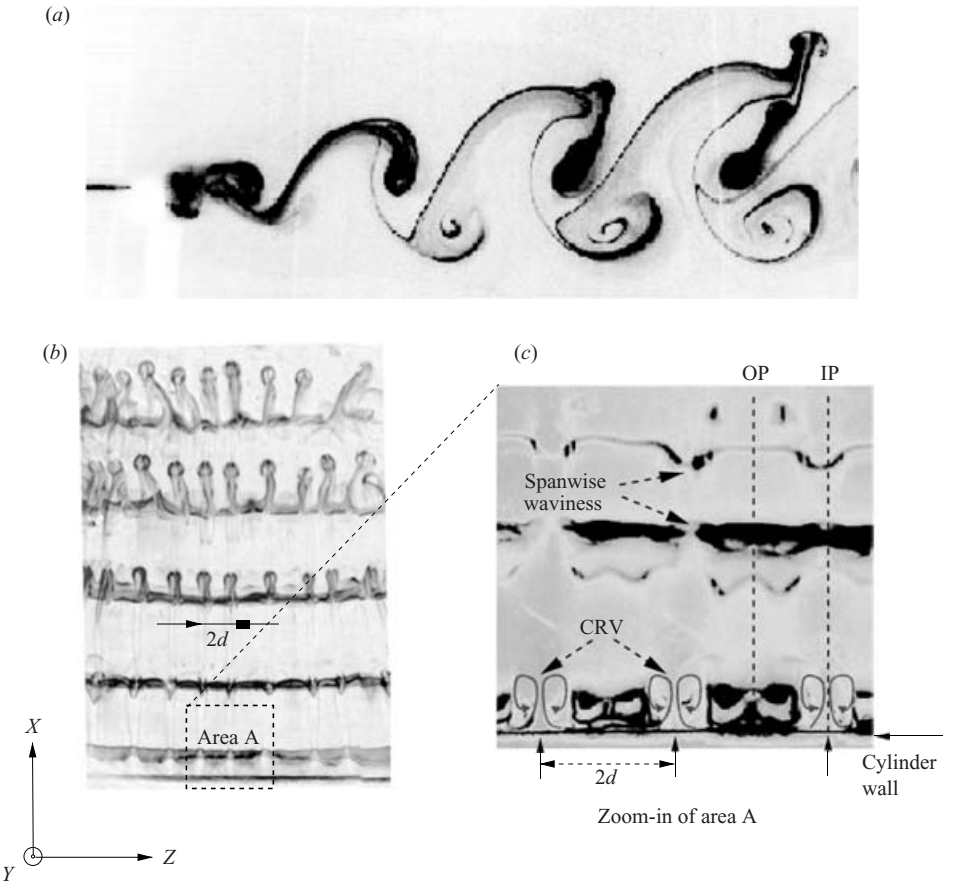

FIGURE 4. (*a*) Side view and (*b*) top view of the wake flow obtained by tin-precipitation visualization at $Re = 117$ and $Ri = 1.0$. (*c*) Flow pattern visualization at $y = 0$ for $Ri = 1.0$ and $Re = 85$. The arrows show the presence of the counter-rotating vortices (CRV). IP and OP indicate the 'in-plume' and 'out-of-plume' positions, respectively. The distance between the 'in-plume' position and the 'out-of-plume' position is one cylinder diameter, after Ren *et al.* (2004*a*).

To gain more insight into the transition mechanism, detailed visualizations are conducted in the near wake. A horizontal laser sheet is created cutting the centreline of the cylinder with the camera positioned perpendicular to this sheet. Figure 4(*c*) shows the flow patterns at $y = 0$ for $Ri = 1.0$ and $Re = 85$. It is observed that pairs of counter-rotating vortices (CRV) appear directly behind the cylinder. These pairs of counter-rotating vortices appear for $Ri > 0.3$ and the strength of the secondary flow increases as the heat input increases. The distance between the CRV is around twice the cylinder diameter. Furthermore, a spanwise waviness is observed both in the vortices and the braids. It is observed that for increasing Richardson numbers, the spanwise waviness in the braids becomes stronger than the one in the primary vortices. The averaged distance between the counter-rotating vortices is around $2d$. It seems that the distance is independent of the Reynolds and Richardson numbers in the range studied: $75 < Re < 117$ and $0.3 < Ri < 2.5$.

Furthermore, in Ren *et al.* (2004*a*), the vortex-shedding process behind a heated cylinder is investigated and the vortex formation shows large differences between the

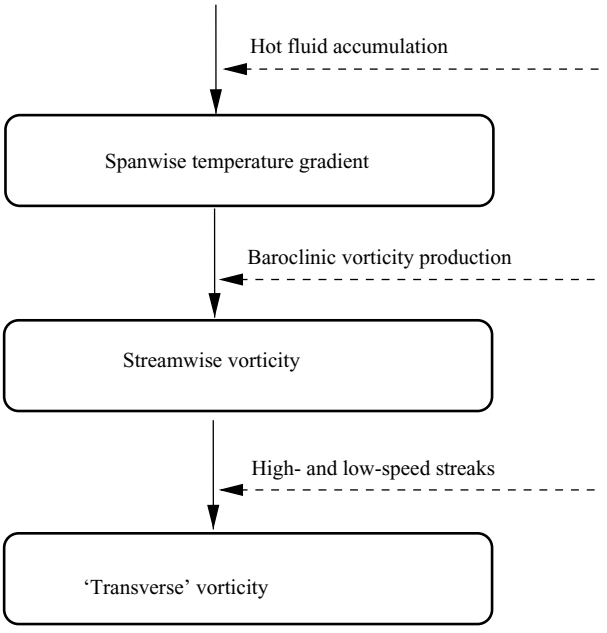

FIGURE 5. Proposed process of coherent structure formation in the near wake.

in-plume position and the out-of-plume position. In figure 4(*c*), IP and OP indicate the in-plume and out-of-plume positions, respectively. The shedding process for the out-of-plume position is similar to the one for an unheated cylinder. For the in-plume positions, the formation of the saddle point in the upper and lower side of the wake is not symmetrical in one vortex-shedding cycle. Furthermore, at the in-plume positions, an upward motion occurs directly behind the cylinder, which separates the vortices from the cylinder wall. An upward motion near the cylinder wall enhances the formation of the upper vortices and weakens the formation of the lower ones.

From the visualization and numerical results, it can be concluded that the spanwise positions of the counter-rotating vortices determine the positions at which the mushroom-type structures escape in the far wake. The observations suggest a strong link between the mushroom-type structures and the coherent structures in the near wake. The proposed formation process can be characterized by three phases (figure 5), which are the occurrence of a spanwise temperature gradient, generation of streamwise vorticity, and generation of 'transverse' vorticity. The occurrence of the spanwise temperature gradient will be discussed in § 4. This spanwise temperature difference leads to the generation of streamwise vorticity, as described in § 5. Next the attention focuses on the generation of transverse vorticity (§ 6). This process repeats itself as a cycle.

4. The three-dimensional temperature field

The flow pattern changes significantly owing to the buoyancy-induced flow (Ren, Rindt & van Steenhoven 2003). To gain insight into the influence of a heat input on the coherent structures in the near wake, the three-dimensional temperature field is studied as a function of time at $Ri = 1.0$ and $Re = 85$.

In figure 6, the numerically calculated three-dimensional iso-temperature surface $\Theta = 0.25$ is presented. It suggests a non-uniform temperature distribution in the

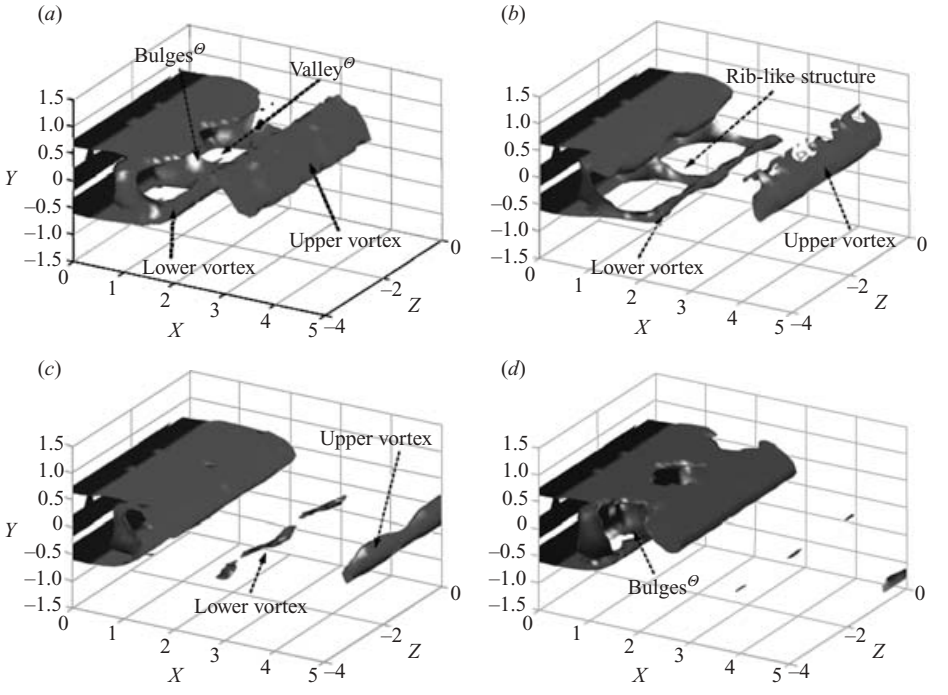

FIGURE 6. Numerically calculated three-dimensional iso-temperature surface $\Theta = 0.25$ as function of time for $Ri = 1.0$ and $Re = 85$. (*a*) $t/T = 0$, (*b*) 1/4, (*c*) 1/2, (*d*) 3/4.

spanwise direction. The fluid in the region marked as 'bulges$^{\Theta}$' has a higher temperature, while the flow marked 'valleys$^{\Theta}$' has a lower temperature. The bulges$^{\Theta}$ and valleys$^{\Theta}$ are formed closely behind the cylinder. They are advected downstream together with the primary vortices. At $t/T = 1/4$, hot fluid has been transported away from the cylinder by the separation of the lower vortices. It is observed that there are rib-like structures at the in-plume positions (figure 6*b*). These rib-like structures evolve from the bulges$^{\Theta}$ mentioned earlier. At $t/T = 1/2$, the temperature distribution of the upper and lower vortex cores are deformed in a spanwise direction (figure 6*c*). Because of the heat diffusion, hot fluid captured in the lower vortices dissipates quickly (figure 6*d*). Meanwhile, new bulges$^{\Theta}$ and valleys$^{\Theta}$ are just formed closely behind the cylinder.

Figure 7(*a*) shows the velocity vectors and temperature fields at $y = 0$. The velocity field shows pairs of counter-rotating vortices occurring behind the cylinder. At the in-plume position, the flow is stagnant, and as a consequence, the fluid around this stagnation region has a high temperature, the so-called bulges$^{\Theta}$. In figure 7(*b*), the temperature distribution in the spanwise direction is presented at different streamwise positions in the 'centre-plane' ($x = 0.5$, $x = 1.0$, $x = 1.5$ and $y = 0$). There is a non-uniform temperature distribution along the spanwise direction. The fluid at the in-plume position has a higher temperature than the fluid at the out-of-plume position. Closely behind the cylinder, at cross-section $x = 0.51$, the spanwise temperature difference between the bulges$^{\Theta}$ and the valleys$^{\Theta}$ is around 0.2 (dimensionless temperature). The spanwise temperature difference becomes less and the temperature decreases in the streamwise direction.

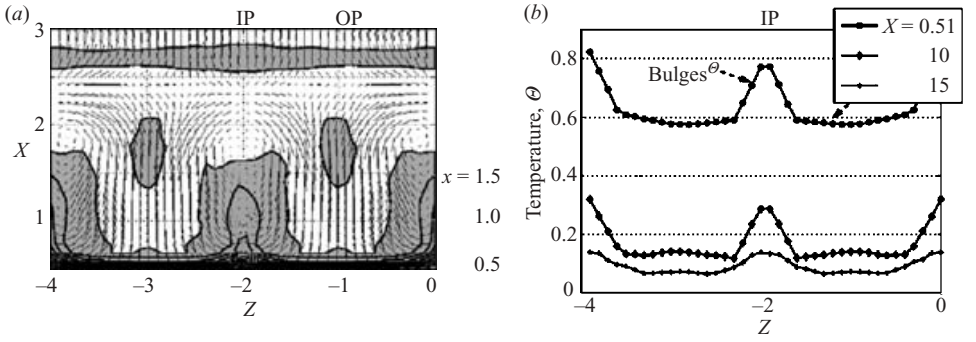

FIGURE 7. The calculated flow pattern at the centreplane of the wake at $t = 2T/4$ for $Ri = 1.0$ and $Re = 85$ using three-dimensional-SEM. (a) The velocity and temperature field at cross-section $y = 0$; (b) temperature profiles at the positions $x = 0.51$, $x = 1.0$, $x = 1.5$ and $y = 0$. IP and OP indicate the in-plume and out-of-plume positions, respectively.

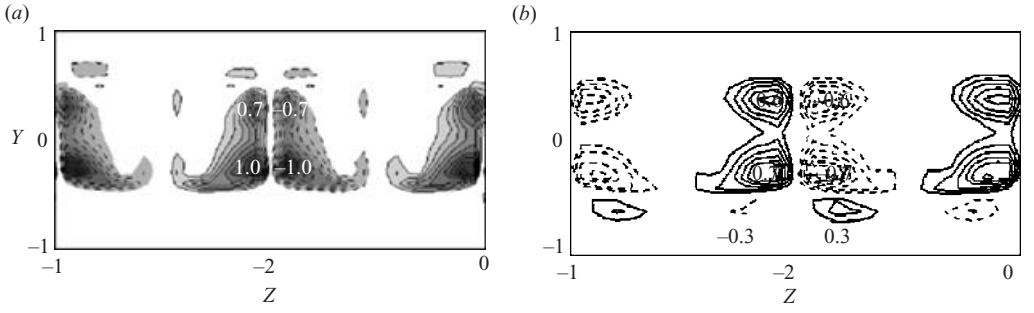

FIGURE 8. (a) Baroclinic vorticity production in the x-direction $\Gamma_x(y, z)$ and (b) streamwise vorticity ω_x at $x = 0.51$ for $Ri = 1.0$ and $Re = 85$.

Figure 8 shows a snapshot of $\Gamma_x = \boldsymbol{\Gamma} \cdot \boldsymbol{e}_x$ (where $\boldsymbol{e}_x$ is the unit vector in the x-direction) closely behind the cylinder, $x = 0.51$. The quantity Γ_x is the production of vorticity in the x-direction due to the baroclinic vorticity torque. From equation (2.4), it follows that $\Gamma_x = -g\, Ri\, \partial\Theta/\partial z$, with $\partial/\partial z$ denoting the gradient in the z-direction. In figure 8(a), regions with positive and negative values of Γ_x are observed around the in-plume position. In Figure 8(b), regions with positive and negative values of ω_x are observed around the in-plume position. The positions of Γ_x and ω_x more or less coincide (figure 8). It can be concluded that the generation of streamwise vorticity in the near wake originates from the baroclinic vorticity production in the x-direction. The fluid has a high temperature at the in-plume position (figure 7). Consequently, an upward motion is induced.

Furthermore, the temperature decreases also in the streamwise direction. Since the density gradient in the streamwise direction is positive in the near wake, additional clockwise spanwise vorticity is created by the production term in the z-direction $\Gamma_z = \boldsymbol{\Gamma} \cdot \boldsymbol{e}_z = g\, Ri\, \partial\Theta/\partial x$. If the baroclinic torque Γ_z has the same sign to the local spanwise vorticity values, the vortices are strengthened. Similarly, if the baroclinic torque Γ_z has the opposite sign to the local vortices, the vortices are weakened. In the near wake, the baroclinic vorticity produced in the z-direction mostly has a negative sign. The production term, therefore, weakens the primary vortices in the lower half of the wake. It is observed that the upper vortices are stronger than the lower ones. This

is in agreement with the observations from two-dimensional numerical simulations by Kieft *et al.* (2003).

5. Streamwise vorticity

5.1. *A global picture*

The generation of streamwise vorticity is due to the temperature difference in the spanwise direction. A study of the evolution of streamwise vorticity will provide more insight into the coherent structure formation in the near wake.

Figure 9 presents the calculated iso-surface $\omega_x = \pm 0.4$ as a function of time at $Re = 85$ and $Ri = 1.0$. Additionally, the iso-surface $\Theta = 0.1$ is shown as a reference to the position of the vortices. The occurrence of streamwise vorticity is observed closely behind the cylinder, and the streamwise vorticity manifests itself as a pair of counter-rotating vortices. For simplicity, the streamwise vortical pair in the vorticity field is referred to as SVP. In figure 9(*a*), the SVP is marked as SVP^+ in the upper half of the wake and SVP^- in the lower half of the wake (figure 9*b*). Additionally, figures 9(*a*)–(*d*) are the corresponding side views of figures 9(*e*)–(*g*), starting from the out-of-plume position ($z = -3$) indicated as OP in figure 9(*e*).

5.1.1. SVP^+

At $t = 0$, the SVP^+ is just formed closely behind the cylinder (figure 9*e*). The SVP^+ is advected together with the shedding of the upper vortices. At $t = T/4$, figure 9(*f*) shows that the SVP^+ moves downstream and encounters the high-speed flow from the upstream of the cylinder (figure 9*b*). At $t = 2T/4$, the upper vortex is cut off owing to the shear flow from the lower side of the wake. The SVP^+ grows both in strength and size (figure 9*g*). The SVP^+ is continuously supplied by streamwise vorticity generated close behind the cylinder. Around $x = 2.0$, the SVP^+ is positioned in a 'neck region' at the upper half of the wake. The neck region is an area with strong shear of the main flow in the y-direction. At $t = 3T/4$, the SVP^+ is cut off owing to the separation of the upper vortex (figure 9*d*). The wake cavity is open and the flow from the upper side of the wake enters the cavity. The legs of the SVP^+ move gradually inwards in the upper braid region. The inward motion has a 'varicose shape' (figure 9*h*).

5.1.2. SVP^-

In figure 9(*c*), the SVP^- has been accumulated at the lower side of the wake. Similar to the SVP^+, the advection of the SVP^- is associated with the shedding of the lower vortex. The SVP^- is stretched into the braid region at the lower half of the wake. In figure 9(*d*), the SVP^- moves downwards and experiences the high-speed flow. The SVP^- continues to grow both in strength and size (figure 9*d*, *a*). In figure 9(*b*), the generated streamwise vorticity is transported downstream along the SVP^-. The vorticity continues to grow until the SVP^- is cut off (figure 9*c*). The tail of the SVP^- runs into the wake centre where the flow is slowed down (figure 9*d*).

5.1.3. $SVP^{\mathscr{U}}$ and $SVP^{\mathscr{L}}$

Besides the streamwise vorticity located in the braid region, streamwise vorticity is also observed inside the vortex core. The streamwise vorticity inside the upper vortices is referred to as $\mathrm{SVP}^{\mathscr{U}}$. In figure 9(*a*), the $\mathrm{SVP}^{\mathscr{U}}$ appears around $x = 1.0$. The $\mathrm{SVP}^{\mathscr{U}}$ is possibly induced by the action of SVP^+ and SVP^-. In figure 9(*b*), the $\mathrm{SVP}^{\mathscr{U}}$ has grown stronger. In figure 9(*c*), the $\mathrm{SVP}^{\mathscr{U}}$ starts to form into the shape of a 'tadpole' (a large head and a long tail). The reason for this is not clear. In figure 9(*d*), the $\mathrm{SVP}^{\mathscr{U}}$

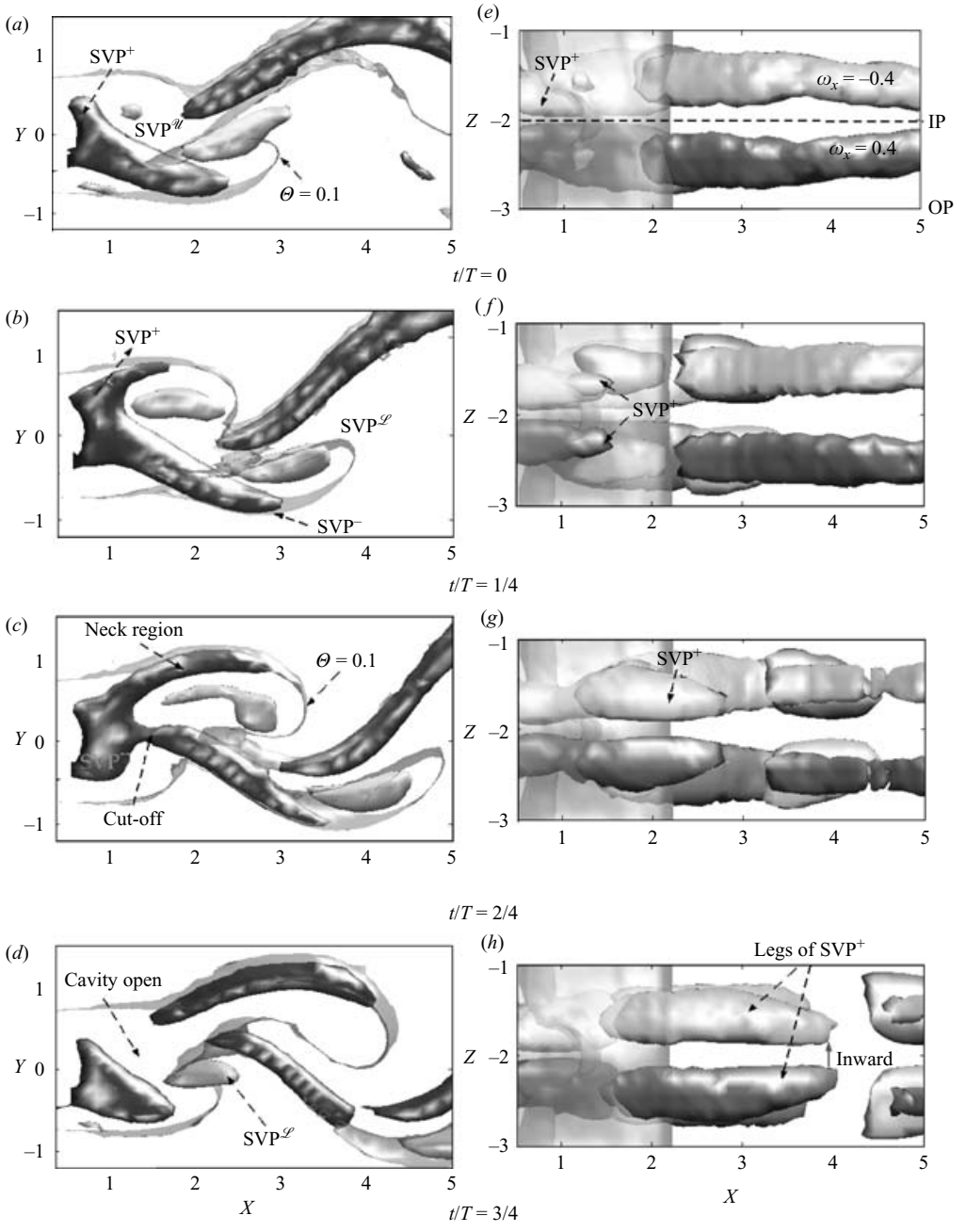

FIGURE 9. Numerically calculated iso-vorticity surface $\omega_x = \pm 0.4$ and iso-temperature surface $\Theta = 0.1$ for $Ri = 1.0$ and $Re = 85$. (*a–d*) Side-view; (*e–h*) top-view of wake. (*a*, *e*) $t/T = 0$, (*b*, *f*) 1/4, (*c*, *g*) 1/2, (*d*, *h*) 3/4. IP and OP indicate the in-plume and out-of-plume positions. SVP, streamwise vortical pair.

seems suddenly to disappear, in a sense that the SVP$^{\mathscr{W}}$ has streamwise vorticity values smaller than $|\omega_x| < 0.4$. The streamwise vorticity inside the lower vortices is marked as SVP$^{\mathscr{V}}$. In figure 9(*d*), the SVP$^{\mathscr{V}}$ appears around $x = 2.0$. The SVP$^{\mathscr{V}}$ is advected downstream, together with the lower vortex.

5.2. *The cross-sectional velocity field*

To gain more insight into the occurrence of the streamwise vortical structures (SVP) discussed above, the flow patterns are shown in cross-section at different streamwise positions. Figure 10 shows the calculated streamwise velocity and secondary velocity fields at $t = 2T/4$ for $Re = 85$ and $Ri = 1.0$. The corresponding streamwise vortical structures are shown in figure 9(*c*). In figures 10(*a*)–10(*e*) contours of the streamwise velocity $\mathscr{U}(y, z)$ are shown at different streamwise positions. The flow direction is out of the paper. Figures 10(*f*)–10(*j*) show the velocity field $[\mathscr{V}(y, z), \mathscr{W}(y, z)]$ at the same streamwise positions.

5.2.1. *Velocity component $\mathscr{U}(y, z)$ at various x-positions*

In figure 10(*a*), the streamwise velocity is almost zero inside the wake cavity region. Outside the wake cavity region, the streamwise velocity is around $\mathscr{U} = 1.0$. In figure 10(*b*), the streamwise velocity profile at the lower side of the wake has a hill-shape. The streamwise velocity at the in-plume position is $\mathscr{U} = 0.005$, while the flow next to the in-plume position has around zero velocity. In figure 10(*c*), the hill-shape disappears from the streamwise velocity profile. A 'bridge' is formed at the in-plume position between the upper and lower side of the wake. The flow inside the bridge has a streamwise velocity of $\mathscr{U} = 0.1$, while the streamwise flow component at the out-of-plume position is around zero. In figure 10(*d*), the streamwise velocity pattern does not change too much. However, the difference in flow speed between the in-plume position and the out-of-plume position becomes slightly larger.

In figure 10(*e*), there is no longer a bridge observed in the streamwise velocity profile. The streamwise velocity at the in-plume position decreases to $\mathscr{U} = 0.005$. The flow becomes slower at the upper half of the wake because for $t = 2T/4$, $x = 2.5$ is located at the centre of the vortex core (figure 9*c*). The flow inside the vortex core is quite slow. Furthermore, a W-shape velocity profile is observed at the lower side of the wake. The wave-shape is associated with an observed convergent flow in the secondary velocity field (figure 10*j*).

5.2.2. *Velocity field $[\mathscr{V}(y, z), \mathscr{W}(y, z)]$ at various x-positions*

Figure 10(*f*) shows, in the velocity field, the occurrence of a secondary flow around the in-plume position at $z = -2$. In figure 10(*g*), counter-rotating flow can be observed which is located around the top of the hill-shape. In figure 10(*h*), an upward motion is observed. This upward motion is around the bridge observed in figure 10(*c*). Furthermore, the upward motion at the in-plume position enhances the velocity magnitude, which is larger than that at the out-of-plume position.

Figure 10(*i*) shows that the secondary motion occurs mostly inside the wake cavity region, while outside the wake cavity region ($|y| > 1$) the secondary flow motion is much smaller. It seems that a crossflow is formed around the boundary of $y = 1.0$. This crossflow may correspond to the neck region in figure 9(*c*).

5.3. *The cross-sectional vorticity field*

Figures 11(*a*)–11(*e*) present the calculated streamwise vorticity contours at different streamwise positions for $Re = 85$ and $Ri = 1.0$. The corresponding streamwise vortical structure is shown at $t/T = 1/2$, as shown in figure 9(*c*).

In figure 11(*a*), closely behind the cylinder, regions of streamwise vorticity (ω_x) are observed around the in-plume position at $z = -2$. The corresponding SVP^+ and SVP^- are symmetrically located at the upper and lower halves of the wake cavity. The maximum strength of the streamwise vorticity is about $\omega_x^{max} = \pm 0.7$ and is located

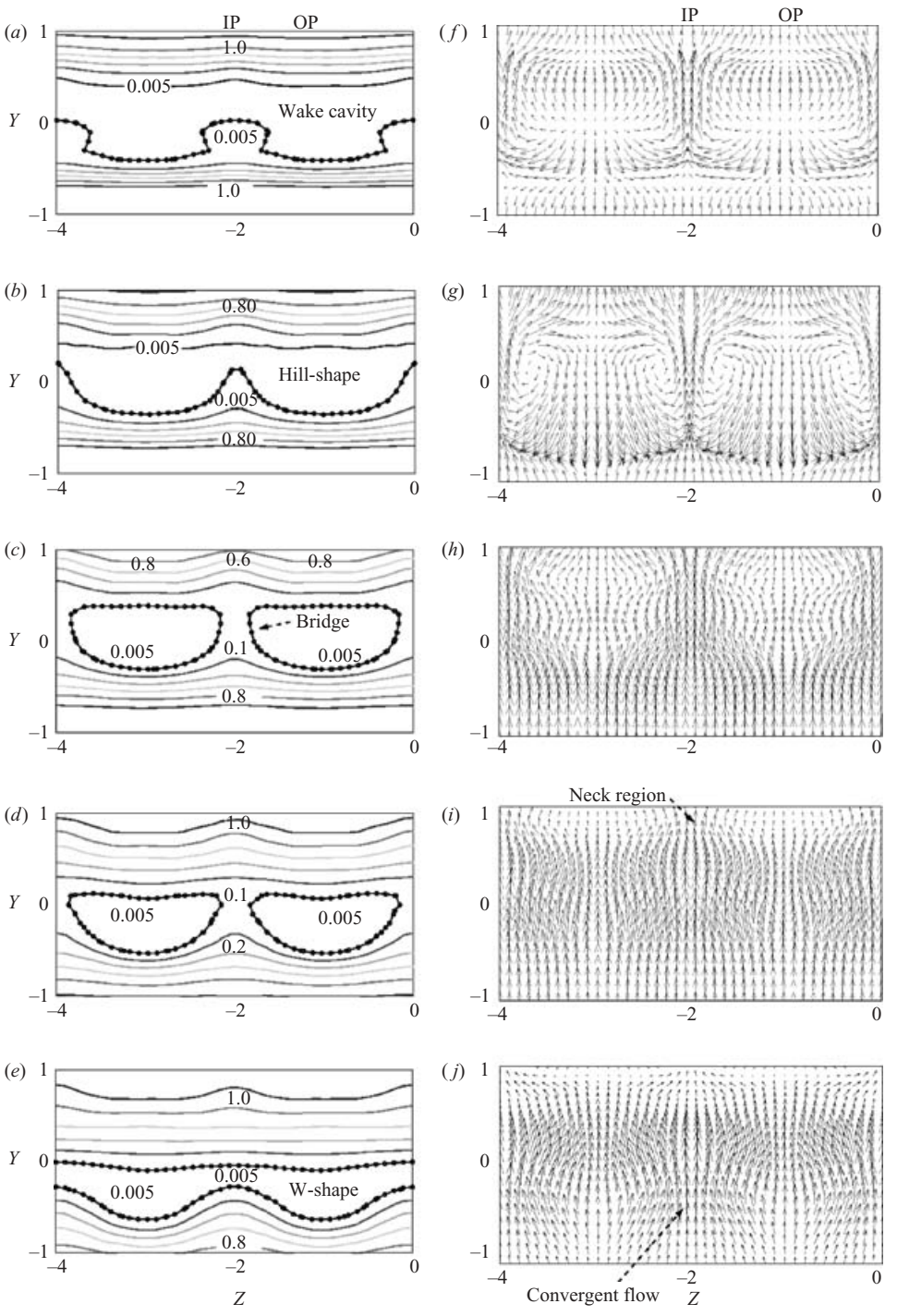

FIGURE 10. The numerically calculated velocity fields for different cross-sections at $t = 2T/4$ for $Re = 85$ and $Ri = 1.0$. (*a–e*) Contours of the streamwise velocity magnitude $\mathscr{U}(y, z)$; (*f–j*) the velocity field $[\mathscr{V}(y, z), \mathscr{W}(y, z)]$. (*a, f*) $x = 0.51$, (*b, g*) 1.0, (*c, h*) 1.5, (*d, i*) 2.0, (*e, j*) 2.5. IP and OP indicate the in-plume and out-of-plume positions, respectively.

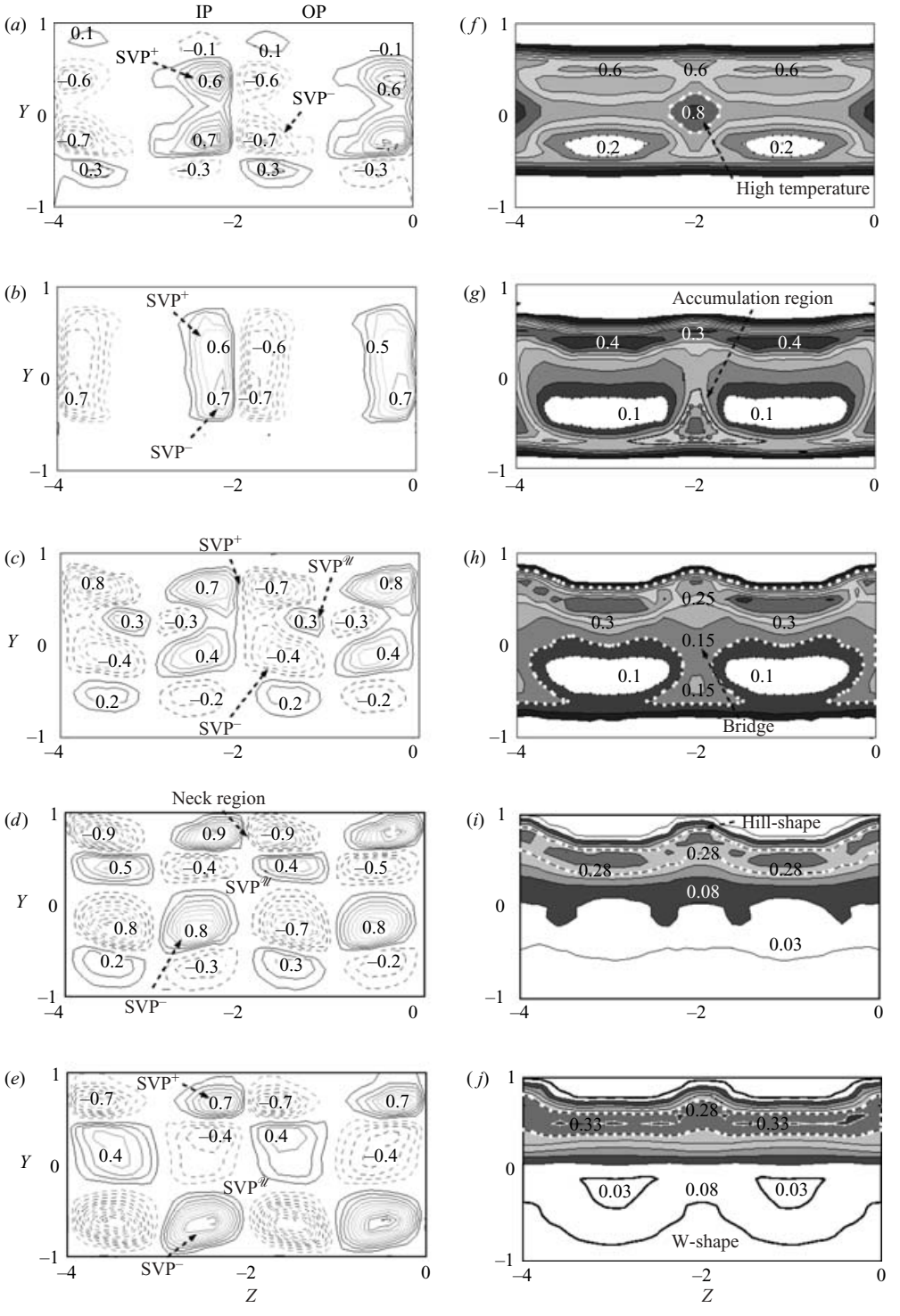

FIGURE 11. The numerically calculated flow pattern for different cross-sections at $t/T = 1/2$ for $Re = 85$ and $Ri = 1.0$. (*a–e*) Contours of the streamwise vorticity $\omega_x(y, z)$; (*f–j*) contours of the temperature $\Theta(y, z)$. (*a*, *f*) $x = 0.51$, (*b*, *g*) 1.0, (*c*, *h*) 1.5, (*d*, *i*) 2.0, (*e*, *j*) 2.5. IP and OP indicate the in-plume and out-of-plume positions, respectively. SVP, streamwise vortical pair.

at the lower side of the wake. Furthermore, alternative rotating streamwise vortices appear outside the wake region, but they are weaker than the streamwise vortices inside the wake cavity. In Figure 11(*b*), the SVP$^+$ and SVP$^-$ seem to join into one coherent structure. The maximum strength of the streamwise vorticity is more or less $\omega_x^{max} = \pm 0.7$. In figure 11(*c*), however, the flow pattern splits into three parts: SVP$^+$, SVP$^-$ and SVP$^{\mathscr{U}}$. The SVP$^+$ is located at the upper braid region, the SVP$^-$ is located at the lower braid region and the SVP$^{\mathscr{U}}$ is located inside the upper vortex. The SVP$^+$ has a vorticity strength of $|\omega_x^{max}| = 0.7$ and the SVP$^-$ of $|\omega_x^{max}| = 0.4$. Between the SVP$^+$ and SVP$^-$, an alternative rotating SVP$^{\mathscr{U}}$ appears with strength $|\omega_x^{max}| = 0.3$. It is associated with the tail of the tadpole-shape of the SVP$^{\mathscr{U}}$ inside the upper vortices (figure 9*c*). At $x = 2.0$, the SVP$^+$ and SVP$^-$ are separated by the SVP$^{\mathscr{U}}$ (figure 11*d*). The maximum strength of the SVP$^+$ is around $|\omega_x^{max}| = 0.9$ and of the SVP$^{\mathscr{U}}$ around $|\omega_x^{max}| = 0.4$. Their magnitudes are both larger than at $x = 1.5$. In figure 11(*e*), the strength of the SVP$^+$ is around $|\omega_x^{max}| = 0.7$ and the SVP$^-$ around $|\omega_x^{max}| = 1.0$. The high strength of the SVP$^-$ is associated with the W-shape observed in the streamwise velocity profile (figure 10*e*) It appeared that for $t = 2T/4$ the SVP$^+$ has its maximum strength of $|\omega_x^{max}| = 0.9$ around $x = 2.0$. The maximum strength of the SVP$^+$ is possibly associated with the SVP$^+$ positioned in the neck region at the upper half of the wake (figure 9*c*). Recalling figure 9(*b*), the SVP$^+$ encounters the high-speed flow from upstream of the cylinder. As a consequence it experiences a positive shear $\partial \mathscr{U}/\partial x > 0$. For $S_{xx} > 0$, therefore, the strength of the streamwise vorticity ω_x increases.

5.4. *The cross-sectional temperature field*

The temperature profiles $\Theta(y, z)$ are given for different streamwise positions. In figures 11(*f*)–11(*j*) the temperature fields are shown for $Re = 85$ and $Ri = 1.0$. The corresponding vorticity fields are shown in figures 11(*a*)–11(*e*).

Figure 11(*f*) suggests that hot fluid is accumulated around the centre of the wake cavity closely behind the cylinder, $x = 0.51$. The fluid with the higher temperature is located around the in-plume position at $z = -2$ (figure 11*g*). Furthermore, there is a region of hot fluid accumulation around the in-plume position. The accumulation of hot fluid creates an unstable stratification in the y-direction. The buoyancy force may become dominant when the temperature difference is large enough. Correspondingly, an upward motion is observed around this region of hot fluid accumulation (figure 10*g*).

In figure 11(*h*), a small-amplitude spanwise waviness in the temperature field can be seen in the upper vortices. There is some kind of 'bridge' at the in-plume position. Through this bridge, hot fluid moves from the lower side to the upper side of the wake. This bridge in the temperature field is related to the bridge observed in the streamwise velocity profile (figure 10*c*). At the upper side of the wake, the temperature at the in-plume position is $\Theta = 0.25$, while the temperature at the out-of-plume position is $\Theta = 0.3$. Thus the temperature difference can be seen between the out-of-plume and the in-plume positions. This is possibly because the cooler fluid from the lower half of the wake cools the fluid at the upper half of the wake via the bridge (figure 10*h*). The temperature in the bridge is around $\Theta = 0.15$.

At position $x = 2.0$, the temperature distribution at the upper side of the wake has a 'hill-shape' (figure 11*i*). The occurrence of the hill-shape is associated with the convergent flow around the neck region (figure 10*i*).

In figure 11(*j*), the temperature distribution, at the lower half of the wake, shows a strong deformation and has a W-shape. The W-shape is located at the lower braid

region. It coincides with the observation that the SVP^- increases in strength at the lower braid region (figure 11*e*).

6. 'Transverse' vorticity

Besides the investigation of the streamwise vorticity, the evolution of the vorticity component in the gravity direction is also studied within the present contribution. This vorticity component ω_y is referred to as the 'transverse' vorticity.

6.1. *The velocity field at* $y = 0$

In figure 12, both measured and calculated velocity fields are shown as a function of time for $Re = 85$ and $Ri = 1.0$. The velocity field is measured at $y = 0$ using the HPV technique. A horizontal laser sheet is cut through the centreline of the wake. The camera is positioned perpendicular to this sheet and the camera is focused within an area of 40 mm × 40 mm. The calculated velocity field is achieved by using a three-dimensional SEM. In figure 12, the details of the velocity field $[\mathscr{U}(x, z), \mathscr{W}(x, z)]$ at $y = 0$ are shown in the near wake.

At $t = 0$, as shown in figures 12(*a*) and 12(*e*), the flow pattern can be divided into two regions: backward flow ($0.5 < x < 2.5$) and forward flow ($2.5 < x < 5$). Closely behind the cylinder, the flow moves back towards the cylinder. In figure 12, the streamwise velocity is almost zero at the in-plume position, while at the other spanwise position the streamwise velocity is strongly negative inside the wake cavity. Both measured and calculated velocity fields show counter-rotating vortices (CRV) at $x = 1$ closely behind the cylinder with a spanwise distance of $2d$.

At $t = T/4$, the flow around the CRV is directed backwards. The distance between these counter-rotating vortices is around two cylinder diameters (figure 12*b*). This flow pattern is coherent with the visualization result shown in figure 4(*b*). In figure 12(*f*), the calculated velocity field shows good agreement with the measured one. At $t = 2T/4$, the CRV moves downstream, although the flow around the CRV has a backward motion. In figure 12(*c*), the flow speed at the in-plume position becomes higher. Differences in streamwise velocity can be seen between the in-plume and the out-of-plume positions. The differences are associated with the spanwise waviness, observed in the visualizations (see figure 4*b*). At $t = 3T/4$, a convergent flow is observed around $x = 3$ at the in-plume position. The differences in streamwise velocity become larger, as shown in figure 12(*d*). The distance between the convergent flows is also two cylinder diameters. In figure 12(*h*), the calculated velocity field shows similar convergent flows. The evolution of the flow structures is determined both experimentally and numerically with a high resolution.

In general, good agreement has been achieved between the three-dimensional SEM calculated and the HPV measured velocity field, although some differences in the velocity field are observed. A possible reason for the difference is that the finite thickness of the laser sheet O (4 mm) limits accuracy in the particle tracking method. Furthermore, in figure 12(*a*, *b*), it can be seen that the centre of the couter-rotating vortices is not located at exactly $Z = -2$. This shift might be due to a background motion in the towing tank.

6.2. *The vorticity field at* $y = 0$

From the velocity field $[\mathscr{U}(x, z), \mathscr{W}(x, z)]$ obtained from the HPV measurements, the transverse vorticity ω_y is derived by $\omega_y = \partial\mathscr{U}/\partial z - \partial\mathscr{W}/\partial x$. Figure 13 reveals the development of ω_y as a function of time for $Re = 85$ and $Ri = 1.0$.

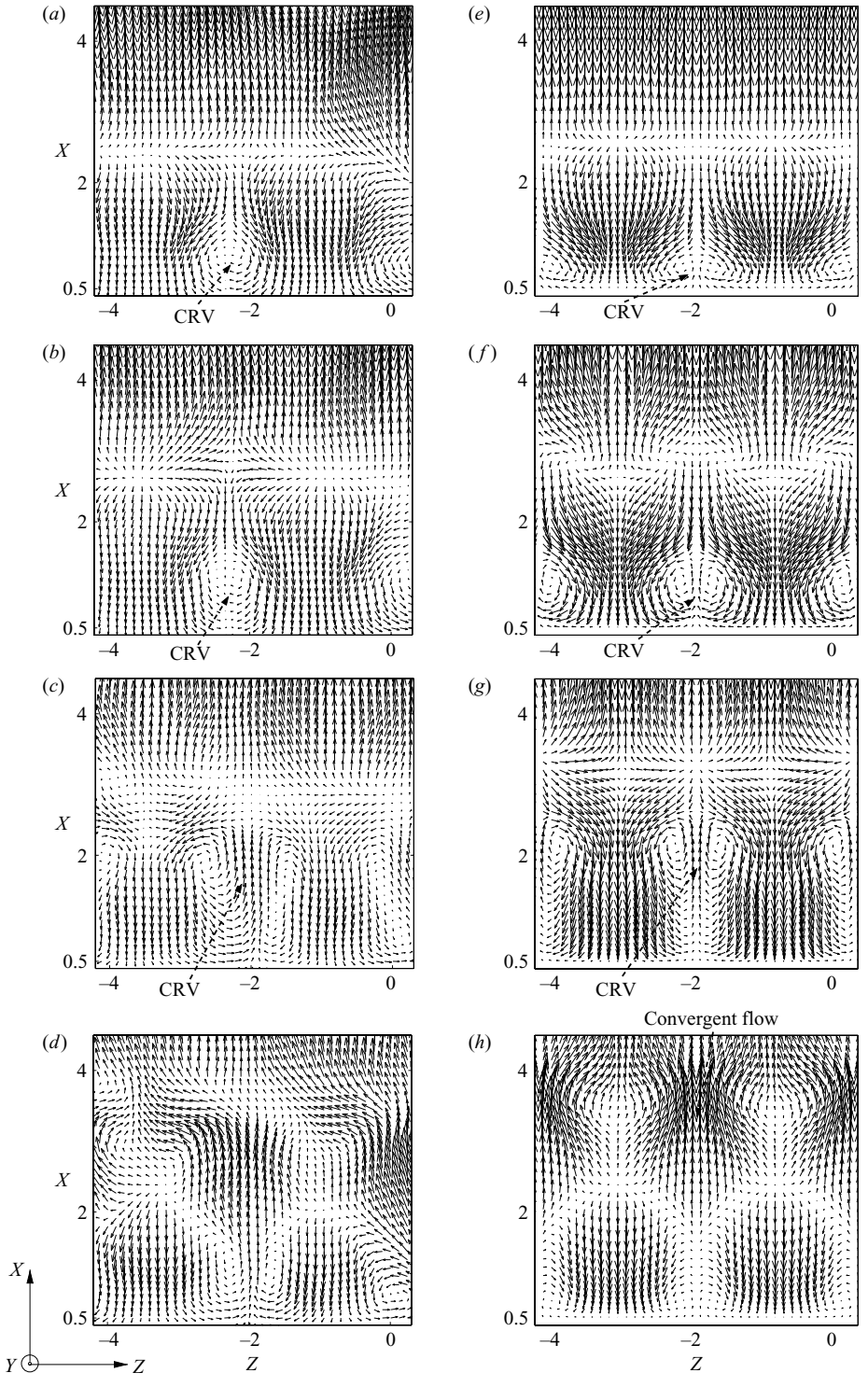

FIGURE 12. Velocity fields as a function of time at $y = 0$ for $Re = 85$ and $Ri = 1.0$. (a–d) The HPV result; (e–h) the three-dimensional SEM result. The flow is from bottom to top and gravity is in the negative y-direction. (a, e) $t/T = 0$, (b, f) 1/4, (c, g) 1/2, (d, h) 3/4. CRV, counter-rotating vortices.

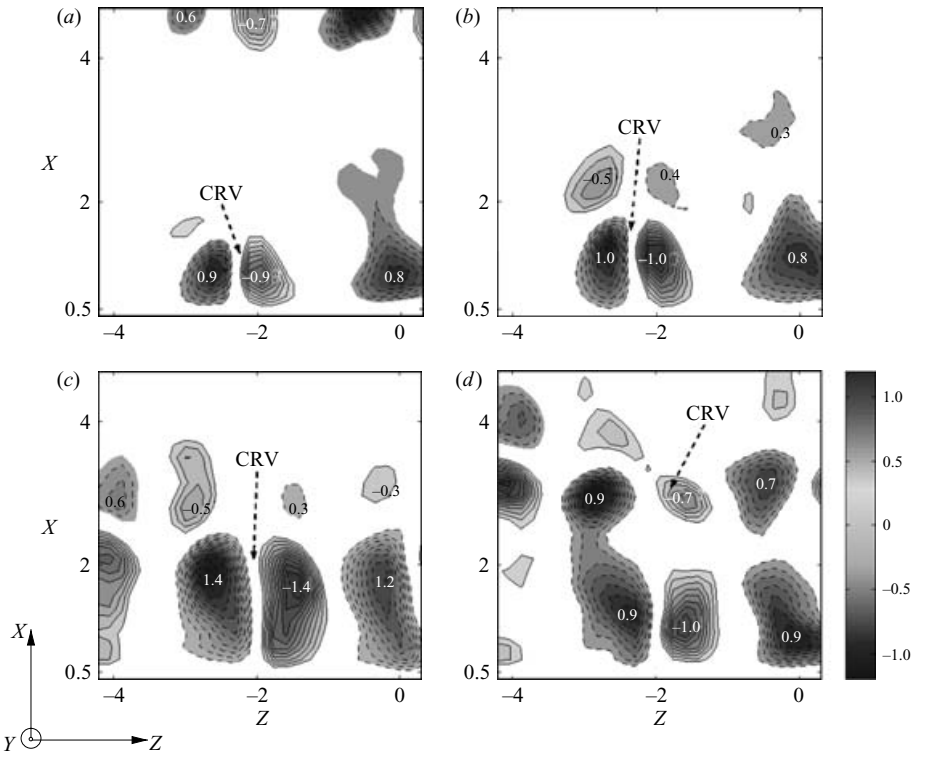

FIGURE 13. Vorticity field ω_y as a function of time for $Re = 85$ and $Ri = 1.0$ obtained by using the HPV technique. The numbers indicate the local maximum values of the vorticity component ω_y. (*a*) $t/T = 0$, (*b*) 1/4, (*c*) 1/2, (*d*) 3/4. CRV, counter-rotating vortices.

In figure 13(*a*), pairs of counter-rotating vortices (CRV) are observed behind the cylinder. The CRV occur roughly at $x = 1$ with a strength of $|\omega_y^{max}| \simeq 0.9$. The distance between the counter-rotating vortices is around twice the cylinder diameter. The strength of the counter-rotating vortices varies with time. At $t = T/4$, the strengths of the CRV are around $|\omega_y^{max}| = 1.0$ (figure 13*b*). At $t = 2T/4$, the CRV occur at roughly $x = 2$ with a strength of $|\omega_y^{max}| = 1.4$ (figure 13*c*). The occurrence of the CRV is observed both in the measured and calculated velocity field figures 12(*c*, *g*). In figure 13(*d*) the strength of the CRV is again around $|\omega_y^{max}| = 0.9$.

6.3. *The streamwise velocity field*

To understand the formation mechanism of the transverse vorticity, ω_y, the time development of the streamwise velocity profile $\mathscr{U}(x, z)$ is studied in the near wake.

6.3.1. *Velocity component* $\mathscr{U}(x, z)$ *at* $y = 0$

In figure 14, the streamwise velocity profiles are presented at $y = 0$. These profiles are obtained both experimentally (figure 14*a–d*), and numerically (figure 14*e–h*). Figure 14 shows that good agreement in flow pattern is achieved between the HPV measurement and three-dimensional SEM calculation, although some differences in the peak value of the streamwise velocity are observed. These differences are possibly due to the finite thickness of the laser sheet O (4 mm), which limits the accuracy in the particle tracking method. The streamwise velocity is obtained by averaging the

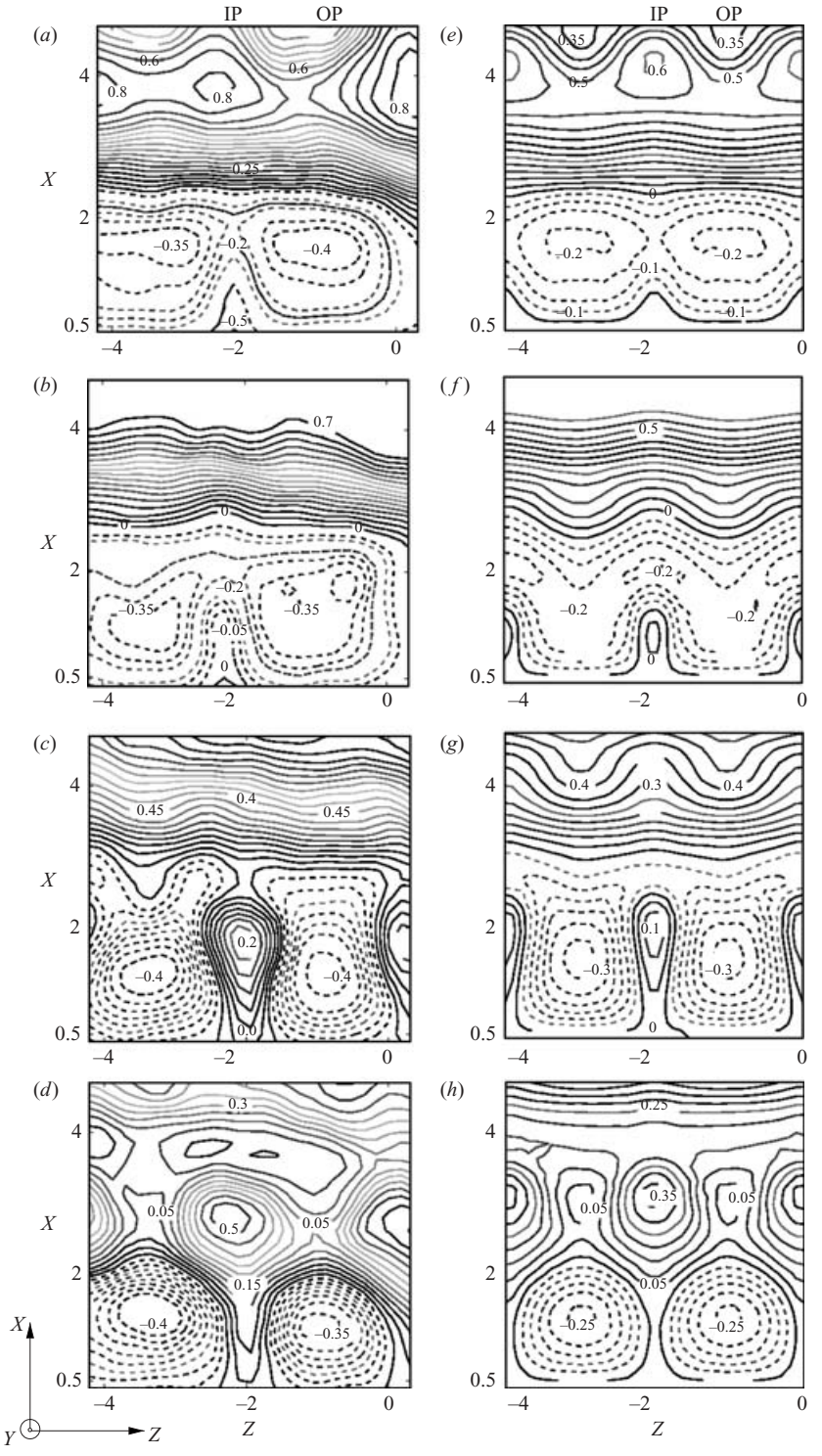

FIGURE 14. The streamwise velocity profile $\mathscr{U}(x, z)$ as a function of time at $y = 0$ for $Re = 85$ and $Ri = 1.0$. $(a-d)$ measured with the HPV technique; $(e-h)$ calculated with three-dimensional SEM. (a, e) $t/T = 0$, (b, f) 1/4, (c, g) 1/2, (d, h) 3/4. IP and OP indicate the in-plume and out-of-plume positions, respectively.

particle path in the laser sheet. The averaged particle path will lead to higher values of the flow velocity.

At $t/T = 0$, around $x = 1$, two circular regions with negative streamwise velocity are observed at the out-of-plume positions (figure 14*e*). Around the in-plume position, the streamwise velocity is almost zero. This suggests that the flow at the in-plume position is more or less stagnant closely behind the cylinder. Similar profiles are observed in the HPV results (figure 14*a*). At $t = T/4$, the streamwise velocity near the cylinder is around $\mathscr{U}^{ip} = 0$ at the in-plume position, while at the out-of-plume position the streamwise velocity is around $\mathscr{U}^{op} = -0.15$ (figure 14*f*). Strong curvature and inflection points are developing in the streamwise profiles near the cylinder. This is correlated to the forward motion at the in-plume position and the backward motion at the out-of-plume position (figure 14*e*). At $t = 2T/4$, the velocity difference between the in-plume and out-of-plume positions becomes larger. The streamwise velocity is around $\mathscr{U}^{ip} = 0.1$ at the in-plume position, while at the out-of-plume position the streamwise velocity is around $\mathscr{U}^{op} = -0.3$ (figure 14*g*). At $t = 3T/4$ around $x = 3$ the streamwise velocity is around $\mathscr{U}^{ip} = 0.25$ at the in-plume position, while at the out-of-plume position the streamwise velocity is around $\mathscr{U}^{op} = 0.05$ (figure 14*h*).

It seems that the flow speed $|\mathscr{U}^{ip}|$ at the in-plume position is always smaller than that $|\mathscr{U}^{op}|$ at the out-of-plume position. In other words, the low-speed streak is located at the in-plume position and the high-speed streak is located at the out-of-plume position. Therefore, the streamwise velocity profile develops two inflection points, which induce vorticity in the transverse direction. The generated counter-rotating vortices (ω_y) are indicated in figure 13. However, the streamwise velocity profiles $\mathscr{U}(x, z)$ are different in the upper and lower halves of the wake. The origin of the difference observed in the vortical structure formation between the upper and lower halves of the wake is investigated. The flow is studied at $Re = 85$ and $Ri = 1.0$ by using three-dimensional SEM.

6.3.2. *Velocity component* $\mathscr{U}(x, z)$ *at* $y = 0.5$

Figures 15(*a*)–15(*d*) present the streamwise velocity profiles $\mathscr{U}(x, z)$ at $y = 0.5$ (upper half of the wake). In Figure 15(*a*), two circular regions are observed around $x = 2$. The circles refer to upward flows intruding into the plane $y = 0.5$ with equal streamwise velocity. The streamwise velocity at the out-of-plume position is around $\mathscr{U}^{op} = 0.4$, while at the in-plume position the streamwise velocity is around $\mathscr{U}^{ip} = 0.25$. It is clear to see that there exists a spanwise-varying shear flow $\mathscr{U}(x, z)$ with high- and low-speed streaks. The occurrence of the high- and low-speed streaks is associated with the formation of the transverse vorticity. In figure 15(*b*), it is observed that the flow speed increases in the near wake, and the difference becomes less between the high- and low-speed streaks. Furthermore, closely behind the cylinder the streamwise velocity is around $\mathscr{U}^{ip} = 0.05$ at the in-plume position, whereas it is around $\mathscr{U}^{op} = 0.1$ at the out-of-plume position.

In figure 15(*c*), the streamwise velocity is around $\mathscr{U}^{ip} = 0.05$ at the in-plume position, while at the out-of-plume positions it is around $\mathscr{U}^{op} = 0.15$. The streamwise velocity along the spanwise direction has a wavy shape. This wavy shape is related with the high- and low-speed streaks in the x-direction. The high- and low-speed streaks lead to the inflection points in the streamwise velocity profile $\mathscr{U}(x, z)$. These inflection points result in the generation of the transverse vorticity. Finally, in figure 15(*d*), the two circular regions begin to appear again and the process repeats itself.

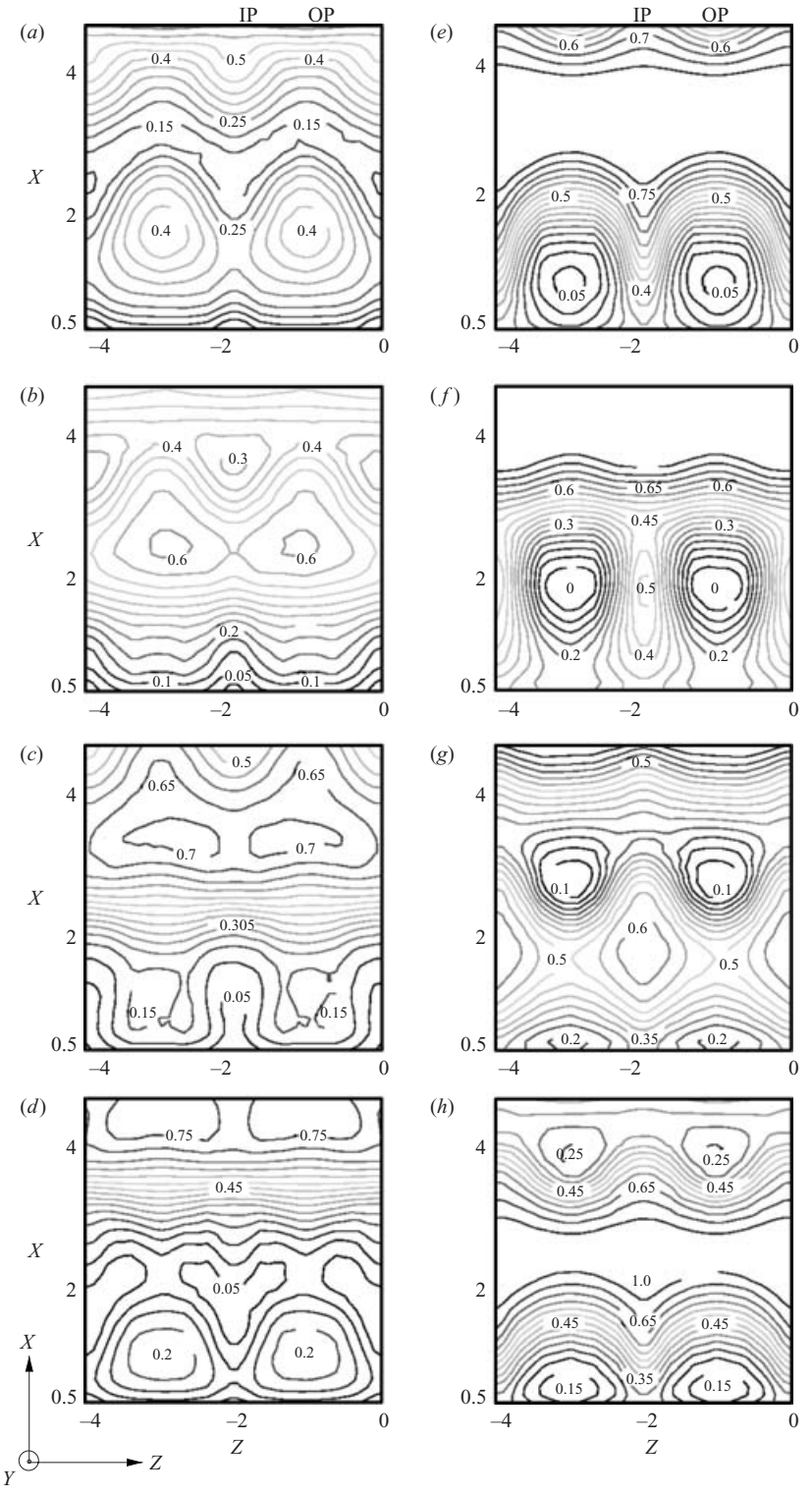

FIGURE 15. The calculated streamwise velocity profile $\mathscr{U}(x, z)$ as function of time for $Re = 85$ and $Ri = 1.0$. (a–d) $y = 0.5$; (e–h) $y = -0.5$. (a, e) $t/T = 0$, (b, f) $t/T = 1/4$, (c, g) 1/2, (d, h) 3/4. IP and OP indicate the in-plume and out-of-plume positions, respectively.

6.3.3. *Velocity component* $\mathscr{U}(x, z)$ *at* $y = -0.5$

Figures 15(*e*)–15(*h*) show the streamwise velocity profiles at $y = -0.5$ (lower half of the wake). At $t/T = 0$, the circular regions are observed closely behind the cylinder. These circles refer to downward flows intruding the plane $y = -0.5$ with equal streamwise velocity. The streamwise velocity at the out-of-plume position is around $\mathscr{U}^{op} = 0.05$, while at the in-plume position the streamwise velocity is around $\mathscr{U}^{ip} = 0.4$. A spanwise-varying shear flow $\mathscr{U}(x, z)$ is shown in figure 15(*e*). The spanwise variance between the in-plume and out-of-plume positions is larger than that at the upper half of the wake (figure 15*a*). At $t = T/4$, the flow speed around the circular regions decreases at the in-plume position, while the flow speed around the out-of-plume positions increases. The streamwise velocity around the circular regions is around $\mathscr{U}^{op} = 0$, while at the in-plume position it is around $\mathscr{U}^{ip} = 0.5$ (figure 15*f*). The spanwise variance in the streamwise velocity profile $\mathscr{U}(x, z)$ becomes larger. Figure 15(*g*) shows a strong spanwise waviness around $x = 2$. The flow for the in-plume position is slower than that for the out-of-plume position. In other words, the high-speed streak is located at the out-of-plume position and the low-speed streak is located at the in-plume position. At $t = 3T/4$, the flow pattern is split into two parts along the line $x = 3$ (figure 15*h*). This 'splitting' is associated with the ambient fluid from the lower side of the wake entering the wake cavity (figure 9*c*). It is a region with more or less constant streamwise velocity $\mathscr{U}(x, z) \simeq 1.0$.

From the streamwise velocity profiles presented in figure 15, the following findings are made. At the upper half of the wake, the high-speed streak is located at the out-of-plume position and the low-speed streak is located at the in-plume position. The difference between the low- and high-speed streaks is defined as $\Delta\mathscr{U}$:

$$\Delta\mathscr{U}|_{y=0.5} = \mathscr{U}^{ip} - \mathscr{U}^{op} < 0 \quad \text{at} \quad y = 0.5. \tag{6.1}$$

However, at the lower half of the wake, the fast-speed streak is located at the in-plume position and the slow-speed streak is located at the out-of-plume position.

$$\Delta\mathscr{U}|_{y=-0.5} = \mathscr{U}^{ip} - \mathscr{U}^{op} > 0 \quad \text{at} \quad y = -0.5. \tag{6.2}$$

This difference in $\mathscr{U}^{ip} - \mathscr{U}^{op}$ between the upper and lower halves of the wake is related with the redistribution of streamwise momentum by the streamwise rolls. There is a similar finding in the study of boundary-layer transition. Waleffe (1995) decomposed the velocity field $[\mathscr{U}, \mathscr{V}, \mathscr{W}]$ into x-independent velocity components $[\mathscr{V}(y, z), \mathscr{W}(y, z)]$ associated with streamwise vorticity and an x-independent streamwise component $\mathscr{U}(y, z)$. The streamwise vorticity, which is associated with $[\mathscr{V}(y, z), \mathscr{W}(y, z)]$, leads to a redistribution in the (y, z)-plane of the streamwise momentum, which is related with $\mathscr{U}(y, z)$.

Furthermore, the sign of function $\Delta\mathscr{U} = \mathscr{U}^{ip} - \mathscr{U}^{op}$ results in different kinds of inflections between the upper and lower half of the wake. The generated transverse vorticity (ω_y) is just opposite for the upper and lower halves of the wake. The occurrence of the transverse vorticity changes the orientation of the streamwise rolls. It is observed that the SVP^+ at the upper half of the wake shows an inward motion, while the SVP^- at the lower half of the wake shows an outward motion.

7. Discussion and conclusions

The three-dimensional flow transition behind a heated cylinder at low Reynolds number, $Re = 85$ and $Ri = 1.0$ (in water), manifests itself in the form of escaping

mushroom-type structures out of the upper vortices in the far wake. To explain this phenomenon, a cyclic-process of the formation of secondary vortical structures in the near-wake has been found. Close behind the cylinder, the presence of a spanwise temperature gradient leads to the generation of streamwise vorticity, which results from baroclinic vorticity production. Because of these streamwise vorticity regions, low-speed flow will move upwards resulting in high- and low-speed streaks in the upper half of the wake. Next, 'transverse' vorticity is generated by the spanwise gradients in the streamwise velocity, resulting in counter-rotating vortices directly behind the cylinder. These vortices lead to high- and low-temperature regions in spanwise direction and the process repeats itself.

I. Spanwise temperature gradient

Closely behind the cylinder, there are regions of hot fluid accumulation around the in-plume positions (figure 11*g*). The accumulation of hot fluid is associated with the presence of counter-rotating vortices in the near-wake (figures 4*b* and 7*a*). At the in-plume position, the flow has a higher temperature, which is referred to as bulges$^{\Theta}$. The formation of the bulges$^{\Theta}$ symbolizes hot-fluid accumulation, which creates a spanwise temperature gradient.

II. Streamwise vorticity

Because of the occurrence of the spanwise temperature gradient, vorticity is generated owing to baroclinic vorticity production $\boldsymbol{\Gamma} = -Ri\nabla\Theta \times \boldsymbol{g}$, according to the vorticity transport equation (2.4). As shown in figures 6 and 7(*b*), the temperature decreases along the spanwise direction from the bulges$^{\Theta}$ to the valleys$^{\Theta}$. Thus, streamwise vorticity is generated owing to the baroclinic vorticity production in x-direction:

$$\Gamma_x = \boldsymbol{\Gamma} \cdot \boldsymbol{e}_x = -gRi\frac{\partial \Theta}{\partial z}. \tag{7.1}$$

As plotted in figure 8, the generated streamwise vorticity is located around the in-plume position ($z = -2$).

III. Transverse vorticity

Between the streamwise rolls, the fluid is lifted up. At the upper half of the wake, low-momentum fluid moves upward at the in-plume position. The upward motion creates a low-speed region in the streamwise velocity profile (figure 16). The low-speed streak occurs at the in-plume positions, which is relatively slower than the flow at the out-of-plume position. The variance in the streamwise velocity profile leads to the generation of transverse vorticity ω_y (figure 16). The generated transverse vorticity is featured as counter-rotating vortices (figure 4*b*).

As can be deduced from the above, the formation process of secondary vortical structures in the near-wake of a heated cylinder is a cyclic process (figure 17). This cyclic process consists of the occurrence of a spanwise temperature gradient, generation of streamwise vorticity and generation of transverse vorticity. These elements are coupled with each other as a cycle.

The generation of streamwise vorticity in the near wake is mainly attributed to baroclinic vorticity production in the near wake. It appears that streamwise vorticity induces the occurrence of transverse vorticity, which consequently leads to spanwise temperature differences. This spanwise temperature gradient leads to streamwise

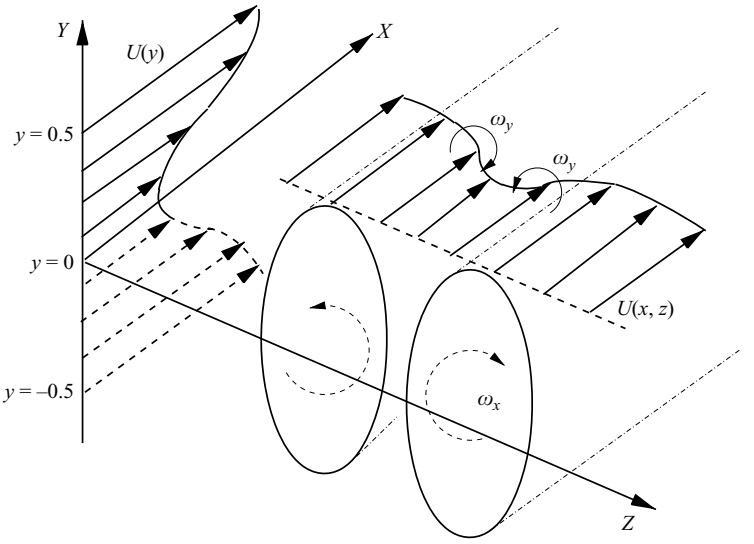

FIGURE 16. Sketch of the transverse and spanwise velocity profiles that form under the influence of streamwise vortices in the wake flow.

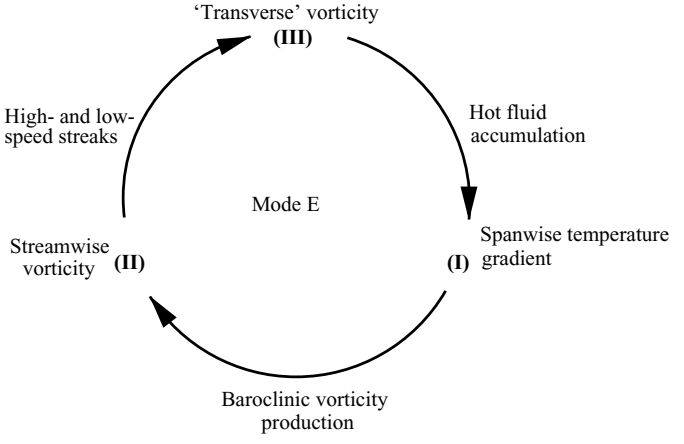

FIGURE 17. A cyclic process close behind the heated cylinder.

vorticity by the action of baroclinic vorticity production. Here, the cyclic process might be related to the mode A instability, which is understood to be a self-sustaining process where previously formed streamwise vorticity affects the formation of new streamwise structures (Williamson 1996*a*).

In the current study, mode E is described in detail and its origin is explained by proposing a cyclic process, in which the importance of baroclinic vorticity production is emphasized. In table 1, the three-dimensional-modes are presented for a cylinder wake flow at relatively low Reynolds numbers together with their characteristic wavelengths. In this table, two other modes, the vortex-adhesion mode and mode C, are not included. The vortex adhesion mode as discovered by Williamson (1992) is characterized by localized vortex dislocations. At these dislocations, the von Kármán vortices seem to adhere to the rear end of the

cylinder wall. In the experiments, vortex-adhesion points are induced by the end conditions for $Re > 160$. Numerical calculations by Zhang *et al.* (1995) showed that the occurrence of this adhesion mode can also arise from instability processes under nominally two-dimensional boundary conditions and is self-sustaining in the range $160 < Re < 230$. Both from simulations and experiments, it is found that another three-dimensional transition mode can be observed by placing a thin wire close to the cylinder and parallel to its axis. This mode is referred to in literature as mode C (Zhang *et al.* 1995) and displays a characteristic spanwise wavelength of around 2 cylinder diameters, which is surprisingly close to that found for mode E. One should realize, however, that mode E occurs at a much lower Reynolds number than mode C. Mode E is found for Reynolds numbers as low as $Re = 75$ as long as the Richardson number is larger than $Ri > 0.35$ (see table 1). Mode C is observed for Reynolds numbers in the range of $170 < Re < 270$. Based on the Floquet stability analysis of Noack & Eckelmann (1994), the critical Reynolds number of this mode is around 170. Another striking resemblance might be that, like mode E, mode C is triggered by introducing a disturbance. In experiments, mode C is mostly excited by positioning one control wire at either side of the cylinder axis. Numerical simulations by Zhang *et al.* (1995) showed that mode C can also be triggered by a symmetric positioning of two control wires with respect to the cylinder axis and even by performing a transversal oscillation of the cylinder with a small amplitude and a frequency corresponding to half the natural shedding frequency. They conclude that the occurrence of mode C is not intimately connected to an asymmetric excitation. In this contribution, mode E is triggered by the action of baroclinic vorticity production in the near wake, which can be considered an asymmetric disturbance. Whether the similar spanwise wavelength of around 2 cylinder diameters for both mode C and mode E is accidental or not will be investigated in the future.

This work is part of the research programme of the Netherlands Foundation for Fundamental Research on Matters (FOM), which is financially supported by the Netherlands Organization for Scientific Research (NWO). The authors would like to thank the secretaries and technical staff of the Laboratory for Energy Technology of the Department of Mechanical Engineering at Eindhoven University of Technology for their support.

REFERENCES

Badr, H. 1984 Laminar combined convection from a horizontal cylinder-parallel and contra flow regimes. *Intl J. Heat Mass Trans.* **27**, 15–27.

Bastiaans, R. J. M., van der Plas, G. A. J. & Kieft, R. N. 2002 The performance of a new PTV algorithm applied in super-resolution PIV. *Exps. Fluids* **32**, 346–356.

Brede, M., Eckelmann, H. & Rockwell, D. 1996 On secondary vortices in the cylinder wake. *Phys. Fluids* **8**, 2117–2124.

Chang, K. & Sa, J. 1990 The effect of buoyancy on vortex shedding in the near wake of a circular cylinder. *J. Fluid Mech.* **220**, 253–266.

Cuvelier, C., Segal, A. & van Steenhoven, A. A. 2001 *Finite Element Methods and Navier–Stokes Equations.* Kluwer.

Hatton, A., James, D. & Swire, H. 1970 Combined forced and natural convection with low-speed air flow over horizontal cylinders. *J. Fluid Mech.* **42**, 17–31.

Honji, H., Taneda, S. & Tatsuno, M. 1980 Some practical details of the electrolytic precipitation method of flow visualization. *Rep. Res. Inst. Appl. Maths* Kyushu University, Fukuoka, Japan **28**, 83–89.

Huerre, P. & Monkewitz, P. A. 1990 Local and global instabilities in spatially-developing flows. *Annu. Rev. Fluid Mech.* **22**, 473–537.

Karniadakis, G. E. & Triantafyllou, G. S. 1992 Three-dimensional dynamics and transition to turbulence in the wake of bluff bodies. *J. Fluid Mech.* **238**, 1–30.

Kieft, R. N. 2000 Mixed convection behind a heated cylinder. PhD thesis. Eindhoven University of Technology, Eindhoven, The Netherlands.

Kieft, R. N., Rindt, C. C. M. & van Steenhoven, A. A. 2002 Heat induced transition of a stable vortex street. *Intl J. Heat Mass Transfer* **45**, 2739–2753.

Kieft, R. N., Rindt, C. C. M., van Steenhoven, A. A. & van Heijst, G. J. F. 2003 On the wake structure behind a heated horizontal cylinder in cross-flow. *J. Fluid Mech.* **486**, 189–211.

Lecordier, J. C., Hamma, L. & Paranthoen, P. 1991 The control of vortex shedding behind heated circular cylinders at low Reynolds number. *Exps. Fluids* **10**, 224–229.

Lecordier, J. C., Browne, L., Le Masson, S., Dumouchel, F. & Paranthoën, P. 2000 Control of vortex shedding by thermal effect at low Reynolds numbers. *Expl Thermal Fluid Sci.* **211**, 227–237.

Maas, W. J. P. M., Rindt, C. C. M. & van Steenhoven, A. A. 2003 The influence of heat on the three-dimensional transition of the von Kármán-vortex street. *Intl J. Heat Mass Transfer* **46**, 3069–3081.

Maday, Y., Paterta, A. & Ronquist, E. 1990 An operator-integration-factor splitting method for time-dependent problems: applications to compressible flow. *J. Sci. Comput.* **5**, 263–292.

Michaux-Leblond, N. & Bélorgey, M. 1997 Near-wake behaviour of a heated circular cylinder: viscosity–buoyancy duality. *Expl Thermal Fluid Sci.* **15**, 91–100.

Mittal, R. & Balachander, S. 1995 Generation of streamwise vortical structures in bluff-body wake. *Phys. Rev. Lett.* **75**, 1300–1303.

Noack, B. R. & Eckelmann, H. 1994 A global stability analysis of the steady and periodic cylinder. *J. Fluid Mech.* **270**, 297–330.

Noto, K. 1991 Computational investigation on wake behavior with buoyancy from a heated elliptic cylinder: effect of mainstream attack angle. In *Proc. Thirty-ninth Japanese National Congress of Applied Mechanic*, pp. 293–303.

Noto, K., Ishida, M. & Matsumoto, R. 1985 A break-down of the von Kármán vortex street due to the natural convection. In *Flow Visualization III* (ed. W. J. Yang), pp. 348–354.

Noto, K. & Matsumoto, R. 1987 Numerical simulation on the development of the von Kármán vortex street due to the negatively buoyant force. In *Proc. Fifth Conf. on Numerical Methods in Laminar Flow*, pp. 796–809. Pineridge.

Pierrehumbert, R. T. 1986 Universal short-wave instability of two-dimensional eddies in an inviscid fluid. *Phys. Rev. Lett.* **57**, 2157–2159.

Ren, M. 2005 3D flow transition behind a heated cylinder. PhD thesis. Eindhoven University of Technology, The Netherlands.

Ren, M., Rindt, C. C. M. & van Steenhoven, A. A. 2003 Buoyancy induced 3D transition behind a heated cylinder. In *Proc. Third Intl Sympm. on Turbulence and Shear Flow Phenomena, Sendai, Japan* (ed. N. Kasagi *et al.*), pp. 717–722.

Ren, M., Rindt, C. C. M. & van Steenhoven, A. A. 2004*a* Experimental and numerical investigation of the vortex formation process behind a heated cylinder. *Phys. Fluids* **16**, 3103–3114.

Ren, M., Rindt, C. C. M. & van Steenhoven, A. A. 2004*b* 3D vortices in the wake flow behind a heated cylinder. *Intl J. Transport Phen.* **6**, 177–187.

van Steenhoven, A. A. & Rindt, C. C. M. 2003 Flow transition behind a heated cylinder. *Intl J. Heat Fluid Flow* **24**, 322–333.

Timmermans, L. J. P., Minev, P. D. & van de Vosse, F. N. 1996 An approximate projection scheme for incompressible flow using spectral elements. *Intl J. Numer. Meth. Fluids* **22**, 673–688.

van de Vosse, F. N., Minev, P. D. & Timmermans, L. J. P. 1995 A spectral element projection scheme for incompressible flow with application to shear-layer stability studies. *Houst. J. Maths* 1284–1291.

Waleffe, F. A. 1990 On the three-dimensional instability of strained vortices. *Phys. Fluids* **2**, 76–80.

Waleffe, F. A. 1995 Hydrodynamic stability and turbulence. *Stud. Appl. Maths* **95**, 319–343.

Wang, A., Travnicek, Z. & Chia, K. 2000 On the relationship of effective Reynolds number and Strouhal number for the laminar vortex shedding of a heated circular cylinder. *Phys. Fluids* **12**, 1401–1410.

Williamson, C. H. K. 1988 The existence of two stages in the transition to three-dimensionality of a cylinder wake. *Phys. Fluids* **31**, 3165–3168.

Williamson, C. H. K. 1992 The natural and forced formation of spot-like 'vortex-dislocations' in the transition of a wake. *J. Fluid Mech.* **243**, 393–441.

Williamson, C. H. K. 1996*a* Three-dimensional wake transition. *J. Fluid Mech.* **328**, 345–365.

Williamson, C. H. K. 1996*b* Vortex dynamics in the cylinder wake. *Annu. Rev. Fluid. Mech.* **28**, 477–539.

Zhang, H. Q., Fey, U., Noack, B. R., Konig, M. & Eckelmann, H. 1995 On the transition of the cylinder wake. *Phys. Fluids* **7**, 779–795.